Biophysical Journal Volume 108 January 2015 325–337

Article

Phosphorylation in the Catalytic Cleft Stabilizes and Attracts Domains of a Phosphohexomutase

Jia Xu,[1] Yingying Lee,[1] Lesa J. Beamer,[1] and Steven R. Van Doren[1,*]
[1]Department of Biochemistry, University of Missouri, Columbia, Missouri

ABSTRACT Phosphorylation can modulate the activities of enzymes. The phosphoryl donor in the catalytic cleft of α-D-phosphohexomutases is transiently dephosphorylated while the reaction intermediate completes a 180° reorientation within the cleft. The phosphorylated form of 52 kDa bacterial phosphomannomutase/phosphoglucomutase is less accessible to dye or protease, more stable to chemical denaturation, and widely stabilized against NMR-detected hydrogen exchange across the core of domain 3 to juxtaposed domain 4 (each by $\geq$1.3 kcal/mol) and parts of domains 1 and 2. However, phosphorylation accelerates hydrogen exchange in specific regions of domains 1 and 2, including a metal-binding residue in the active site. Electrostatic field lines reveal attraction across the catalytic cleft between phosphorylated Ser-108 and domain 4, but repulsion when Ser-108 is dephosphorylated. Molecular dynamics (MD) simulated the dephosphorylated form to be expanded due to enhanced rotational freedom of domain 4. The contacts and fluctuations of the MD trajectories enabled correct simulation of more than 80% of sites that undergo either protection or deprotection from hydrogen exchange due to phosphorylation. Electrostatic attraction in the phosphorylated enzyme accounts for 1) domain 4 drawing closer to domains 1 and 3; 2) decreased accessibility; and 3) increased stability within these domains. The electrostriction due to phosphorylation may help capture substrate, whereas the opening of the cleft upon transient dephosphorylation allows rotation of the intermediate. The long-range effects of phosphorylation on hydrogen exchange parallel reports on protein kinases, suggesting a conceptual link among these multidomain, phosphoryl transfer enzymes.

INTRODUCTION

Phosphorylation regulates enzymes with diverse consequences ranging from long-range allosteric activation of glycogen phosphorylase to million-fold inhibition of isocitrate hydrogenase (1). Phosphorylation of the activation loop of many eukaryotic protein kinases triggers electrostatic rearrangement of the loop and assembly of the internal regulatory spine of hydrophobic residues in the N- and C-lobes of these proteins, thereby supporting interaction with substrate and activity (2). Phosphorylation has been proposed to stabilize proteins by decreasing the range of motions, typically with global conformational adjustments of <2 Å (3); however, exceptions to this stabilization have been noted (4).

α-D-phospho-hexomutases are also sensitive to phosphorylation. Their reaction cycles oscillate between serine phosphorylated and dephosphorylated forms (5–7) (Fig. 1). The serine donates a phosphoryl group to the phosphosugar substrate. While it is transiently dephosphorylated, the serine accepts a phosphoryl group from the bisphosphorylated intermediate (Fig. 1). The phosphorylated enzyme binds and unbinds the phosphorylated sugar, and the bisphosphorylated intermediate reorients by 180° while it is associated with the dephosphorylated enzyme (6,8,9). An attractive member of the enzyme superfamily for biophysically characterizing the effects of phosphorylation on catalytic switching is phosphomannomutase/phosphoglucomutase (PMM/PGM) from *Pseudomonas aeruginosa*.

The phosphomutase activity of PMM/PGM contributes to the infectivity of *P. aeruginosa* in ventilator-assisted pneumonia, chronic obstructive pulmonary disease, and cystic fibrosis (10–12) through the biosynthesis of sugar precursors of lipopolysaccharide, the exopolysaccharides Pel and Psl, rhamnolipids, and alginate (13–16). Ser-108 of PMM/PGM is phosphorylated at the base of a deep, positively charged catalytic cleft formed by its four domains (see Fig. 3 *B*). Upon binding of a phosphosugar, domain 4 (D4) rotates to close the catalytic cleft (9,17). Structures containing a bisphosphorylated intermediate suggested a half-open state of the enzyme (9), which may accommodate the 180° reorientation of the intermediate required by the catalytic cycle (8). ^{15}N NMR relaxation indicates partial independence of the rotational mobility of D4 (18), consistent with crystallographic snapshots of varying conformers of D4 (9). Amide NMR spectra suggest a mixture of phosphorylated and dephosphorylated enzyme forms (18). The catalytic cleft was widened by the S108A mutation (6), suggesting a role for phosphorylation of Ser-108 in conformational adjustment.

The conformational effects of phosphorylation can be investigated by hydrogen exchange (HX, broadly referring

---

Submitted April 23, 2014, and accepted for publication December 3, 2014.

*Correspondence: vandorens@missouri.edu

Editor: Nathan Baker.

0006-3495/15/01/0325/13 $2.00

http://dx.doi.org/10.1016/j.bpj.2014.12.003

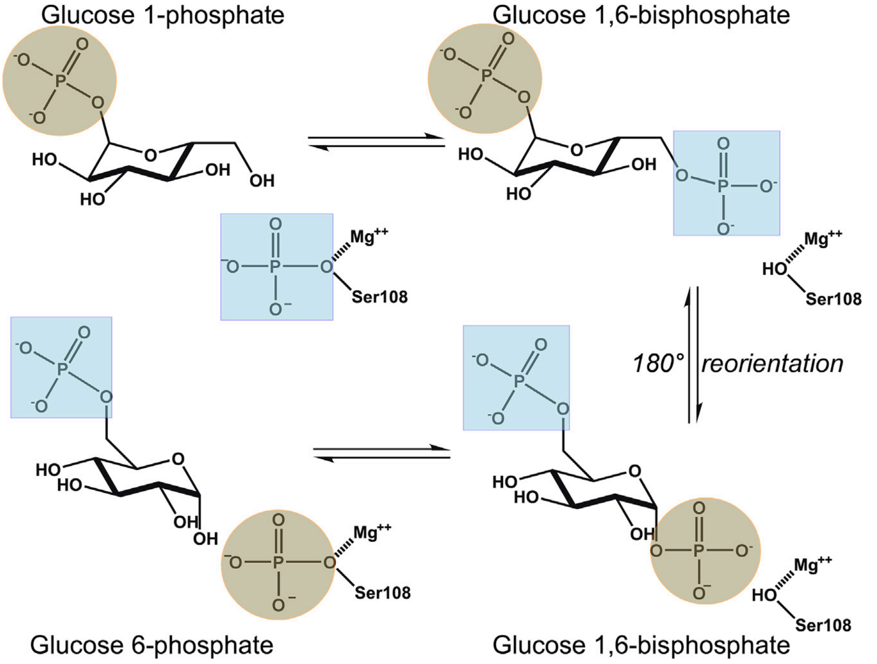

FIGURE 1 Catalytic mechanism of PMM/PGM. The enzyme transforms G1P to G6P via G1,6P, which undergoes rotation in the active site. To see this figure in color, go online.

to fast to slow timescales), which depends on the stability of the structural environment and the longevity of the hydrogen bonds (H-bonds). Transient openings of H-bonds facilitate access of hydroxide ions to amide protons to catalyze exchange. Previously, hydrogen-deuterium exchange mass spectrometry (HDX-MS) revealed percentage changes in the deuteration of peptide fragments of PMM/PGM, suggesting that its dephosphorylated form (Apo-deP) is more flexible than the phosphorylated form (Apo-P), consistent with a role in facilitating the 180° rotation of the intermediate (19). However, limitations inherent to HDX-MS precluded characterization of important aspects of HDX in this enzyme, including regions critical for function. Much of the active site could not be characterized because 1) the peptide containing catalytic phosphoSer-108 was missing from mass spectra; and 2) affected residues in four other peptides encompassing the active site could not be pinpointed due to peptide lengths of 24–35 residues. Residue-specific information was also missing elsewhere. Moreover, HDX-MS data were not available for timescales of seconds or days (20). Consequently, the HDX-MS results did not provide the detailed kinetic and thermodynamic insights required for a biophysical understanding (21).

We implemented NMR to measure HDX and millisecond-scale HX of 463-residue PMM/PGM to pinpoint the effects of phosphorylation on HX as well as its rate constants and free energies. We found that phosphorylation causes both slowing and acceleration of HX around the active site and in D1 and D2, little change at many residues, and slowing of HX of ~100 residues widely and remotely. The sites that are most protected against HDX, as identified by NMR, report the global folding stability (22). This provides a lower limit for the phosphoryl stabilization of the fold of PMM/PGM and its domains, where traditional denaturation experiments fail for lack of reversible folding. Based on changes in the free energy of HX and the density of protected residues, the core of D3 appears to be most protected by phosphorylation, followed by the proximal face of D4. A biophysical accounting for the latter remote pattern of protection by phosphorylation is provided by electrostatic fields and molecular dynamics (MD) trajectories. Comparative calculations for Apo-P and Apo-deP suggest that compaction results from electrostatic attraction introduced by phosphorylation of catalytic Ser-108, i.e., electrostriction. The use of surrounding contacts and either H-bonding or root mean-square fluctuation $(\mathrm{RMSF})^{-1}$ from the MD trajectories (23,24) proved to be qualitatively highly consistent with the locations of altered HX protection accompanying dephosphorylation. The solution and computational lines of evidence reveal what x-ray diffraction constrained by crystal packing (19) could not, i.e., that electrostatic changes due to phosphorylation appear to narrow the active site of PMM/PGM, compact the fold, and slow HX in D3 and D4. These changes may facilitate the capture and accommodation of phosphohexose substrates during the multistep reaction of the enzyme.

MATERIALS AND METHODS

Enzyme preparation

His-tagged PMM/PGM from *P. aeruginosa* was prepared (18). Samples were labeled with ^{2}H and ^{15}N for NMR. The enzyme was phosphorylated to 85–90% or dephosphorylated to 90–95% by incubation with excess glucose 1,6-bisphosphate (G16P) or glucosamine 1-phosphate (Sigma-Aldrich, St. Louis, MO), respectively, at 4°C for 18 h (19).

Accessibility measurements

Apo-P and apo-deP (10 μM), with 90% and 0% levels of phosphorylation, respectively, were incubated with 1 mM of 1-anilinonaphthalene-8-sulfonate (ANS, Fisher, Pittsburgh, PA) for 1 h in 50 mM MOPS (pH 7.4, Fisher) at 25°C. Fluorescence was excited at 365 nm. The fluorescence emission of free ANS in buffer was subtracted away (25).

Then, 30 μM Apo-P and apo-deP, at 87% and 10% levels of phosphorylation, respectively, were treated with proteinase K in 50 mM MOPS (pH 7.4) at a 300:1 (w/w) ratio at 25°C until the reaction was terminated with 3 mM phenylmethylsulfonyl fluoride (MP Biomedicals, Santa Ana, CA). Bands on SDS-PAGE (25) were quantified using ImageJ.

NMR spectroscopy

Band-selective excitation short-transient transverse relaxation-optimized spectroscopy (BEST-TROSY) (26) and other NMR spectra were collected at 35°C on a Bruker Avance III 800 MHz spectrometer with TCI cryoprobe. Samples were incubated in 50 mM MOPS (pH 7.4 at 25°C), 1 mM $MgCl_2$ (Fisher), and 10 mM dithiothreitol (DTT, Gold Biotechnology, St. Louis, MO). The spectra were processed with NMRPipe (27) and peaks were interpreted using Sparky (28) with the reported assignments (18). An in-house-written Python script mapped Sparky-assigned peak shifts to NMRPipe peak tables and is available in the Supporting Material. NMRPipe provided the volume and height of each peak.

Rapid HX by NMR

HX occurring on the millisecond scale was observed using the phase-modulated clean chemical exchange (CLEANEX-PM) pulse sequence enhanced with TROSY detection (29,30) but with interleaved acquisition (see Supporting Material). The solvent-exchange rates were fitted to the equation

$$\frac{I}{I_0} = \frac{k_{ex}}{R_{1A} + k_{ex} - R_{1B}} \times \{\exp(-R_{1B}\tau_m) - \exp[-(R_{1A} + k_{ex})\tau_m]\}, \tag{1}$$

where I/I_0 represents normalized peak heights, R_{1A} is the relaxation rate constant during the spinlock, k is the rate constant of HX, and R_{1B} is the relaxation rate constant for the water (Fig. S2). Radiation damping complicated measurement of R_{1B}. Since trial values of R_{1B} from 0.1 to 0.001 s^{-1} provide the same fitted rate constants (31), a value of 0.01 s^{-1} was used.

Quantification of rates of HDX

Ensuring the uniformity of phosphorylation and dephosphorylation, and keeping the cysteine residues reduced for a week prevented mixtures and biexponential changes. To initiate HDX, $^2H/^{15}N$-labeled samples were concentrated to ~5 mM in H_2O-based buffer and then diluted 5-fold in D_2O-based buffer at 22°C. Addition of 10 mM DTT and Ar to the samples (then sealed in Shigemi tubes) maintained reproducible TROSY spectra for 1 week (judged in H_2O). The 20 min of dead time for these handling steps limited measurable k_{obs} to $< 5 \times 10^{-2}$ min^{-1}. A series of at least 57 BEST-TROSY spectra (26) were acquired at 35°C, continuously during the first 24 h and then several per day until ~8000 min had elapsed. After the first 24 h, the samples were maintained at 35°C in a water bath between acquisitions. Exponential decay rates, k_{obs}, were fitted to the peak heights (Fig. 2 *D*), with correction for the residual 20% H_2O described by Eq. S1 in the Supporting Material. Monitoring of gradual concurrent dephosphorylation and correction of the affected rate constants of HDX (k_{ex}) are detailed in the Supporting Material.

Each intrinsic rate constant of random coil HX (k_{rc}) was obtained using the SPHERE server (http://www.fccc.edu/research/labs/roder/sphere/sphere.html). The free energy of amide protection from HX was calculated as

$$\Delta G_{HX} = -RT\ln(k_{ex}/k_{rc}). \tag{2}$$

The folding stabilities of each domain and the entire enzyme were estimated from the highest values of ΔG_{HX} in each domain and corrected for proline isomerization (22).

Electrostatic field calculations

Atomic charges and sizes around the metal-binding site were parameterized by the Amber tools module MCPB/MTKPP, which invokes Gaussian 2009 (32,33). In the structure of Apo-P (6) (Protein Data Bank (PDB): 1K35), Zn^{2+} is bound by phosphoSer-108 and Asp-242, Asp-244, and Asp-246. In Apo-deP (PDB: 4MRQ) (19), a bound water replaces Ser-108 in coordinating Zn^{2+}. Other atomic sizes and charges were defined by the Amber ff99SB force field (34). The electrostatic potentials were then computed using the Adaptive Poisson-Boltzmann Solver (35) at 310 K with protein and solvent dielectric constants of 2.0 and 78.5, respectively, and ionic strength of 30 mM. Electrostatic field lines were visualized using VMD (36) as described previously (37,38).

Modeling HX protection from MD simulations

The logarithm of the simulated HX protection factor, $\ln(P_n^{sim})$, of an amide group (of residue *n*) can be approximated by linear combination of its number of contacts N_n^c and a second protection factor element (PFE_2) measured from a dynamics simulation, e.g., either the number of H-bonds N_n^h or the $RMSF^{-1}$ at that site:

$$\ln\left(P_n^{sim}\right) = \beta_c N_n^c + \beta_2 \mathrm{PFE}_2, \tag{3}$$

where the generic term $\beta_2 \mathrm{PFE}_2$ can be either $\beta_h N_n^h$ *or* $\beta_{RMSF} RMSF^{-1}$, with the weights of the terms being β_c and either β_h or β_{RMSF} (23,24). For application below, two independent pairs of weight parameters were optimized for slower and faster regimes of HX:

$$\begin{cases} \beta_c^{\mathrm{more\ \ prot}}, \ \ \beta_2^{\mathrm{more\ \ prot}} & \mathrm{if}\ \ \ln\left(\mathrm{P_n^{exp}}\right) > 8 \\ \beta_c^{\mathrm{less\ \ prot}}, \ \ \beta_2^{\mathrm{less\ \ prot}} & \mathrm{if}\ \ \ln\left(\mathrm{P_n^{exp}}\right) < 8 \end{cases}.$$

The modeling of protections improved using the alternative sets of coefficients (Table S3; Fig. S11). The performance of candidate sets of parameters with PMM/PGM is given in Table S4. Simulated protection factors were converted into free energies using Eq. 2: $\Delta G_n^{sim} = -RT\ln(P_n^{sim})$. For details of HX protection simulated from the MD trajectories, see Supporting Materials and Methods.

RESULTS

We investigated phosphorylation-induced changes between the Apo-P and Apo-deP states of PMM/PGM from *P. aeruginosa* in solution and computationally to better understand the interplay of these enzyme forms with the catalytic cycle.

Phosphorylation decreases accessibility to probes and enhances stability

Several approaches were used to compare the overall structural flexibility, openness, and stability of Apo-P and

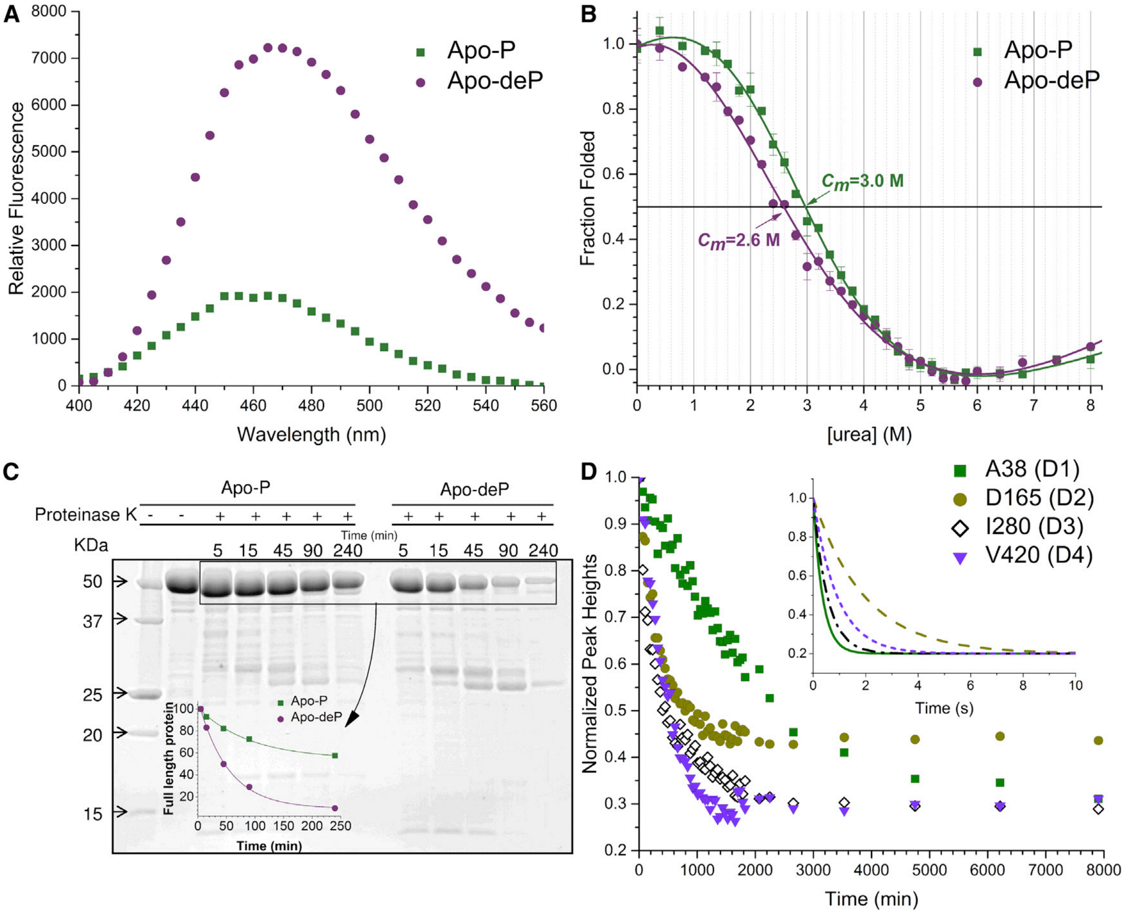

FIGURE 2 Phosphorylation effects on the accessibility and stability of PMM/PGM. (*A*) ANS emission spectra with Apo-P and Apo-deP. (*B*) Apo-P and Apo-deP were denatured by incubation in urea for 12 h at 25°C in 50 mM MOPS, pH 7.4, and 0.1 mM DTT. The intrinsic Trp fluorescence at each point was measured in duplicate. (*C*) Effect of proteinase K on Apo-P and Apo-deP. Aliquots were removed at the indicated times and monitored with SDS-PAGE. The inset plots the decay of the intact enzyme. (*D*) Examples of an amide group in each domain with HX slowed by phosphorylation. The disappearance of an amide peak of each domain from TROSY spectra upon a change of Apo-P to D_2O solution is plotted. The inset shows subsecond components of HX simulated using the rate constants fitted to CLEANEX time courses for the same four residues in the Apo-deP form (Fig. S1). To see this figure in color, go online.

Apo-deP in solution. ANS dye has long been used to probe the conformational changes of proteins because it fluoresces little in water but much more upon binding to a protein (25,39). ANS has a significantly greater fluorescence emission when mixed with Apo-deP than when mixed with Apo-P (Fig. 2 *A*). This suggests that phosphorylation decreases ANS access to binding pockets. We compared the folding stabilities of Apo-P and Apo-deP using urea denaturation. The unfolding curves with [urea] of 3.0 M needed for 50% denaturation (C_m) of Apo-P suggest that it has greater stability than Apo-deP with a C_m of 2.8 M (Fig. 2 *B*). (C_m values are compared here because PMM/PGM cannot be refolded after denaturation, indicating a lack of the reversibility needed to obtain ΔG_{fold}.) Limited proteolysis by proteinase K degrades Apo-deP 6.3-fold faster than it degrades Apo-P, based on rate constants fitted to the disappearance of the intact enzyme band on gels of $2.4 \times 10^{-3} \pm 0.4 \times 10^{-3}$ min^{-1} for Apo-P and $1.5 \times 10^{-2} \pm 0.2 \times 10^{-2}$ min^{-1} for Apo-deP (Fig. 2 *C*). Binding of the small dye, proteolysis by the large enzyme, and urea denaturation suggest that phosphorylation curbs the accessibility of PMM/PGM and enhances its folding stability.

Effects of dephosphorylation on NMR spectra

Time-dependent changes in NMR spectra and mass spectra (loss of the mass of a phosphoryl group) revealed that PMM/PGM undergoes spontaneous dephosphorylation at physiological temperatures (Fig. S2). We performed a residue-by-residue structural comparison of the phosphorylation-dependent changes in accessibility and stability using NMR. Amide peaks representing active Apo-P and Apo-deP forms proved distinguishable for 98 residues with good sensitivity (Fig. S2; Table S1). At 35°C, the NMR peaks of Apo-deP appeared and those of Apo-P disappeared (Fig. S2, *C* and *D*) with a time constant of 19.0 ± 1.1 h (1140 ± 70 min) in the joint fits of the pairs of peaks of 43 residues.

Most of the amide NMR peaks that were shifted by dephosphorylation were distributed from D1 to D3 (Fig. S3, *A* and *B*). Lys-219 of D2, and Arg-262 and Trp-336 of D3 underwent the largest peaks shifts (with $\Delta\omega_{\mathrm{HN}} > 0.2$ ppm) despite being >19 Å distant from the phosphoryl group of Ser-108 (Fig. S3 *B*). In addition, dephosphorylation was found to broaden at least 33 amide peaks beyond detection, with other amide peaks of Apo-deP also being broader than their counterparts in Apo-P, especially in D2 and D3, but also D4 (Figs. S3 and S4). The line broadening probably arises from exchange among structural environments in these domains enabled by dephosphorylation, one manifestation of its long-range effects.

To investigate whether phosphorylation affects the backbone flexibility of PMM/PGM on the scale of picoseconds to nanoseconds, we measured $^{15}\mathrm{N}\{^{1}\mathrm{H}\}$ nuclear Overhauser effect (NOE) relaxation on multiple freshly phosphorylated or dephosphorylated samples. Twenty or more loops and termini showed locally decreased NOE ratios indicating fast, localized fluctuations (Fig. S5). The high similarity of the NOEs of Apo-P and Apo-deP, without differences beyond the standard deviation (SD) of the triplicate measurements, suggests no convincing phosphorylation-dependent change on the subnanosecond scale. Coupled with the much slower millisecond dynamics in Apo-deP implied by its NMR line broadening (Figs. S3 and S4), this suggests the need to test whether the phosphorylation state instead affects more rigidly structured regions, where the conformational resistance may influence dynamics on slow timescales accessible by HX methods.

Slowing of HX by phosphorylation, especially in D3 and the adjacent face of D4

To scrutinize the working hypothesis that dephosphorylation globally mobilizes and increases the accessibility of the structure of Apo-deP (19) (Fig. 2), we performed residue-specific and thermodynamic quantification of HX using NMR. A pH of 7.4, which is needed for solubility and activity of PMM/PGM, and a temperature of 35°C, which enhances its TROSY NMR spectra, promote HX that is intrinsically comparatively rapid. The majority of amide protons were replaced by deuterons within 20 min after exposure to D_2O, especially in Apo-deP (Movie S1). After 1–3 h of exchange, however, more than 100 amide groups across Apo-P appeared to be slowed in HX (Movie S2) relative to Apo-deP, suggesting that multiple locales are stabilized by phosphorylation of the enzyme (Figs. 2 *D*, 3, and S6).

Comparisons of the effects of phosphorylation status on the thermodynamics of HX, i.e., ΔG_{HX}, are newly furnished by these NMR studies of PMM/PGM, for both its individual amide groups and entire domains, provided that its HX occurs in the bimolecular (EX2) limit. In the EX2 regime, the rate of closing of the H-bond (k_{cl}) greatly exceeds the intrinsic rate of HX of a free amide of that residue, k_{rc} (40), in the Linderström-Lang model of HX (41):

$$\mathrm{NH_{closed}} \underset{\mathrm{k_{cl}}}{\overset{\mathrm{k_{op}}}{\rightleftharpoons}} \mathrm{NH_{open}} \xrightarrow{\mathrm{k_{rc}}} \mathrm{ND}. \tag{4}$$

EX2 behavior is recognizable from ΔG_{HX} values shared across a wide range of k_{rc}, and from a slope of 1 among such residues in log-log plots of k_{ex} versus k_{rc} (42,43). Groups of PMM/PGM residues that share similar $\Delta G_{HX,\mathrm{apparent}}$ values do indeed have slopes of 1 in such plots, for both the Apo-P and Apo-deP forms (Fig. S7). This strongly suggests that EX2 behavior prevails for both states of the enzyme, from the slowest-exchanging residues with $\Delta G_{HX} > 10$ kcal/mol through sites of faster exchange with ΔG_{HX} of ~6 kcal/mol (Fig. S7). The EX2 behavior validates the application of Eq. 2 to PMM/PGM to estimate its ΔG_{HX} values from HDX experiments and the stability of H-bonding implied.

Phosphorylation induces stabilization of HX that is significant in segments of D1 and D2, and throughout D3 and D4, as depicted by differences in ΔG_{HX} in Fig. 3. Phosphorylation stabilizes HX by 1.5–9.3 kcal/mol at 35°C (with slowings of 12-fold to 3.8 million-fold) in ~23 residues in D1, 12 residues in D2, 32 residues in D3, and 28 residues in D4 (Fig. 3 *A*). The greatest density of phosphorylation-stabilized residues occurs in the core of D3 throughout its central helix (Leu-263–Ser-273) and the two flanking β-strands (Ala-278–Phe-282 and Leu-322–Gly-324, with 10 phosphorylation-stabilized residues between them). In D4, two long, central β-strands that face D3 (Gly-416–Ala-422 and Arg-432–Glu-434) are similarly stabilized (Fig. 3 *B*). This suggests that phosphorylation may promote closer packing of D4 against D3.

Additional phosphorylation-dependent stabilization $\Delta\Delta G_{HX,P\text{-}deP}$ appears to radiate outward from the most stabilized cores of D3 and D4. Next to the stabilized core helix of D3 are two helices spanning Ile-291–Ser-295 and Ala-347–Ser-354 that also show phospho-stabilization (Fig. 3 *B*). Adjacent to the latter helix, a loop from D2 (Asp-165–Met-173) is similarly stabilized. In D4, additional stabilized residues are found in a stretch from Asp-370 to Thr-381 that contains two β-strands, and in the solvent-exposed helices from Lys-385–Leu-392 and Leu-441–Arg-449 (Fig. 3 *B*). D1 manifests phosphorylation-dependent stabilization $\Delta\Delta G_{HX,P\text{-}deP}$ in a β-strand that faces the active site and phosphoSer-108 (Asn-115–Ile-119), in the adjoining loops, and at the N-terminal ends of two helices within the Val-23–Glu-30 and Leu-59–Lys-66 segments (Fig. 3 *B*). In total, ~15 residues of D1 within 20 Å of the phosphoryl group of phosphoSer-108 are protected by phosphorylation (Fig. 3 *B*).

Twenty amide groups of Apo-P, mainly in D1 and D3, were found to exchange so slowly that the full amplitude of their ΔG_{HX} values could not be determined due to the

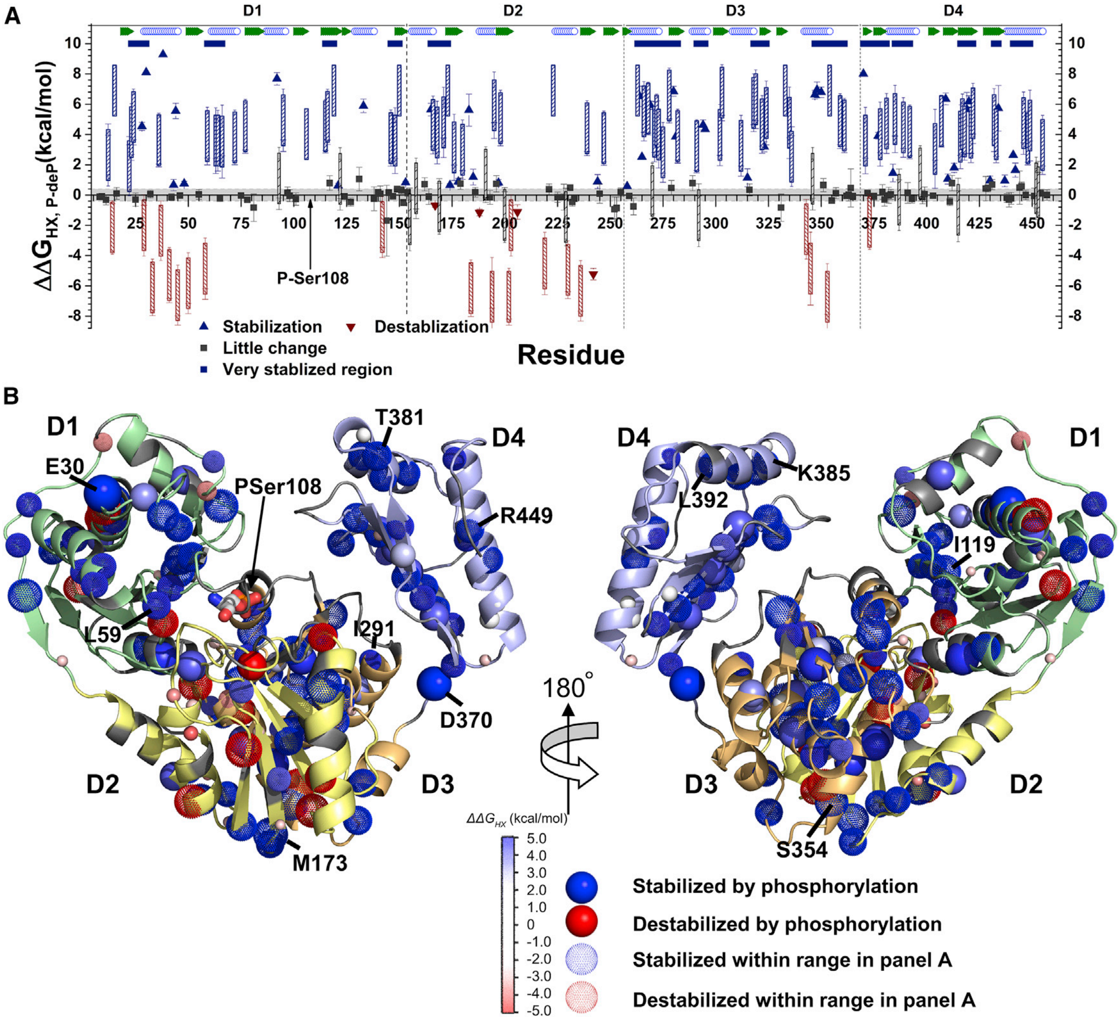

FIGURE 3 Phosphorylation stabilizes or slows HX at more sites than it accelerates. (*A*) Rate constants of HX, k_{ex}, measured either as HDX by NMR or on the subsecond scale by CLEANEX-PM (29), were transformed to ΔG_{HX} using Eq. 2 and the $\Delta\Delta G_{HX,P\text{-}deP}$ differences are plotted. Blue indicates where phosphorylation is significantly stabilizing, and red indicates where it is destabilizing. Triangles represent cases in which k_{ex} was measured in both Apo-P and Apo-deP forms. Hatched bars mark cases in which k_{ex} in one phosphorylation state lay in the intermediate, unmeasured time range where $1\ s^{-1} > k_{ex} > 4 \times 10^{-3}\ s^{-1}$; the height of the bar indicates $\Delta\Delta G_{HX,P\text{-}deP}$ lies within this range. Sequence segments with more than four of 10 residues protected by phosphorylation >2 SD above average are marked with navy blue bars. Locations of strands and helices are given in green and open blue symbols, respectively. (*B*) Amide groups protected from HX by phosphorylation of Ser-108 are marked by spheres with shades of blue, and amide groups destabilized by phosphorylation are in red. Dotted spheres correspond to residues with the uncertainty ranges marked in (*A*). The amplitude of the phosphorylation-dependent change, $\Delta\Delta G_{HX}$, is symbolized by the color intensity and radii of the spheres. To see this figure in color, go online.

gradual, concurrent dephosphorylation of the sample (τ = 19.0 h; see above and Fig. S2). Consequently, it is the lower bound for ΔG_{HX} that is estimated for these 20 groups (*open squares* in Fig. S6) after correction for the slow dephosphorylation (Fig. S8 *A*). Since the HX of Apo-P and Apo-deP lies in the EX2 regime, the most slowly exchanging sites with the largest ΔG_{HX} values can be used to estimate folding stability (44). Applying this method to PMM suggests at the very least a 0.4 kcal/mol greater folding stability of Apo-P ($\geq$11.0 kcal/mol) compared with Apo-deP (10.6 kcal/mol). Local stabilizations by phosphorylation are much greater (Fig. 3 *A*), especially in D3 and D4, where Apo-P appears to be stabilized by at least 1.3 kcal/mol over Apo-deP (Fig. S9). The increased stability from phosphorylation may accompany increases in the conformational rigidity of the protein. This is consistent with the dozens of peaks of Apo-deP that are lost or weakened by line broadening (Fig. S3). These observations may be attributable to chemical exchange among conformers at locations in D3 and D1 in the absence of phosphorylation.

In contrast to the above behaviors, we find sites in D1 and D2 that are locally destabilized by phosphorylation. Specifically, nine residues in D1 and 11 in D2 show HX accelerated by phosphorylation. At least five of these residues in D1 and seven in D2 are destabilized by >1.5 kcal/mol (Fig. 3 *A*). The bulk of the phospho-destabilization in D1 is found within the first helix and the subsequent two loops (Fig. 3). Phosphorylation-destabilized residues are scattered throughout D2.

The NMR studies presented here provide a new opportunity to assess HX around the active site of PMM/PGM. One of the D2 residues destabilized by phosphorylation is Asp-242, which coordinates the divalent cation in the active site. HDX by NMR shows that Asp-242 is well protected in Apo-deP, with $\Delta G_{HX,deP} = 7.3 \pm 0.3$ kcal/mol (Fig. 3 *A*). However, it is strongly destabilized in Apo-P, where its HX is rapid and detected by CLEANEX-PM. This might suggest partial repulsion between the phosphoryl and aspartyl carboxylate groups, which could perturb the metal-binding loop. Ala-184 of D2 and Ile-343 of D3, both within 5 Å of the metal-binding loop, are destabilized in Apo-P as well. In contrast, phosphorylation of Ser-108 stabilizes against HX the amide groups of neighboring residues Thr-106, Asn-115, and Gly-116 of D1, as well as Val-183 and Arg-247 of D2, each within 8 Å of Ser-108.

Phosphorylation attracts D4, whereas dephosphorylation repels D4

The pattern of increased protection from HX due to phosphorylation led to the hypothesis that the negative charge of phosphoSer-108 at the base of the catalytic cleft could 1) attract the positively charged walls of D1 and D4 surrounding the cleft; and 2) draw movable D4 closer to phosphoSer-108 and D3. We tested this by calculating electrostatic field lines and MD trajectories for structures of both Apo-P and Apo-deP. First, we carefully simulated the partial charges on the atoms around the divalent cation-binding site, and near Ser-108 with and without phosphorylation. Many of the electrostatic interactions between domains revealed by the field lines are similar between Apo-P and Apo-deP. However, the phosphorylation of Ser-108 in D1 profoundly alters at long range the charge on the face of D4 and the negative charge in D1 and D2, as evidenced by field lines that converge to the negative potential near the metal-binding site near Val-248 and Gly-249 in D2 (Fig. 4 *C*). In contrast, Apo-deP switches to electrostatic repulsion between these sites in D2 and D4 (Fig. 4 *D*) due to the increased positive charge of its catalytic cleft and metal-binding region. This gives rise to the diverging field lines that are characteristic of repulsion (Fig. 4 *D*). Several other charged residues on the surface of Apo-P appear to form favorable long-range interactions between D1 and D4 or between D2 and D4, which are absent in Apo-deP. Such favorable field lines in Apo-P, which are lost in Apo-deP, include those between Ala-11 (+) and Asp-383 (−), between Thr-426 (+) and both Val-22 and Asp-113 (−), and between Thr-426 (+) and both Phe-210 and Glu-221 (−) (Fig. 4, *A* and *B*). Since D4 is attracted to D1 and D2 in Apo-P, it is likely to contact the intervening D3 more snugly when it rotates toward D1 and D2.

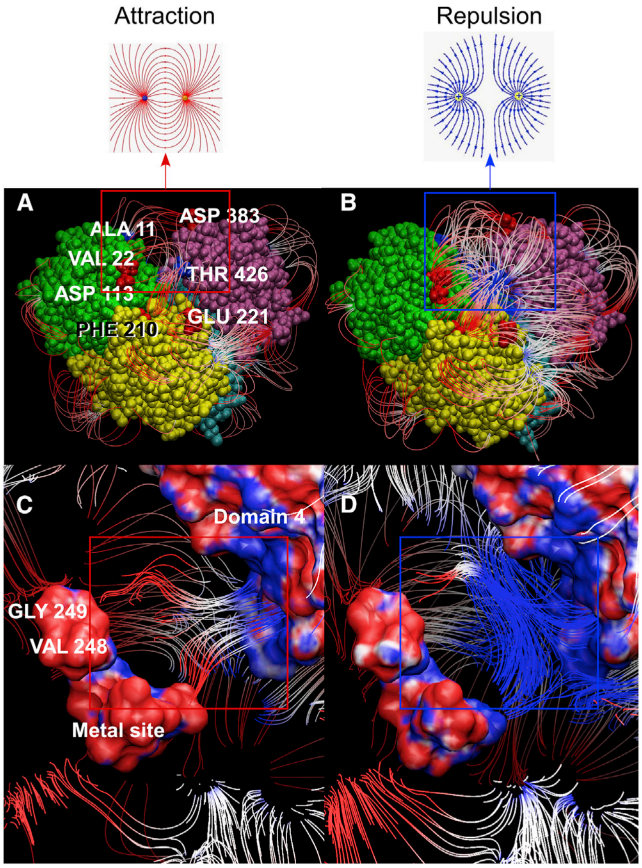

FIGURE 4 (*A–D*) D1 and D4 are electrostatically attracted when Ser-108 is phosphorylated (*A* and *C*), but repelled when it is dephosphorylated (*B* and *D*). (*A* and *B*) D1–D4 are colored green, yellow, cyan, and pink, respectively. (*A–D*) Electrostatic field lines of Apo-P (*A* and *C*) and Apo-deP (*B* and *D*). (*C* and *D*) Expansions of the catalytic cleft highlight attraction and repulsion between D1 and D4 in the red and blue boxes, respectively. To see this figure in color, go online.

MD suggests compaction due to phosphorylation and more freedom without it

To test the working hypotheses that 1) D3 and proximal areas of the other domains are stabilized in their H-bonding (higher ΔG_{HX}); and 2) phosphorylation draws D4 with D3, we compared Apo-P and Apo-deP forms by MD. The force field integrates the long-range electrostatics with van der Waals and covalent interactions. The crystal structures of Apo-P and Apo-deP share identical angles of orientation (73.2°) and distances of separation (28.2 Å) of D4 as defined by Fig. 5, *A* and *D*. The energies and root mean-square deviations from the starting structures stabilized in 5 ns. The distributions of angles and distances were tabulated from this equilibration through the end of the 120 ns trajectories (Fig. 5).

After 18 ns and 60 ns in the simulation, Apo-deP increased in separation of D4 from D1–D3 and from Apo-P (Fig. 5). In Apo-P, the angle defined between the centers of mass of D4 and D1–D3 with a vertex at the D3-D4 hinge

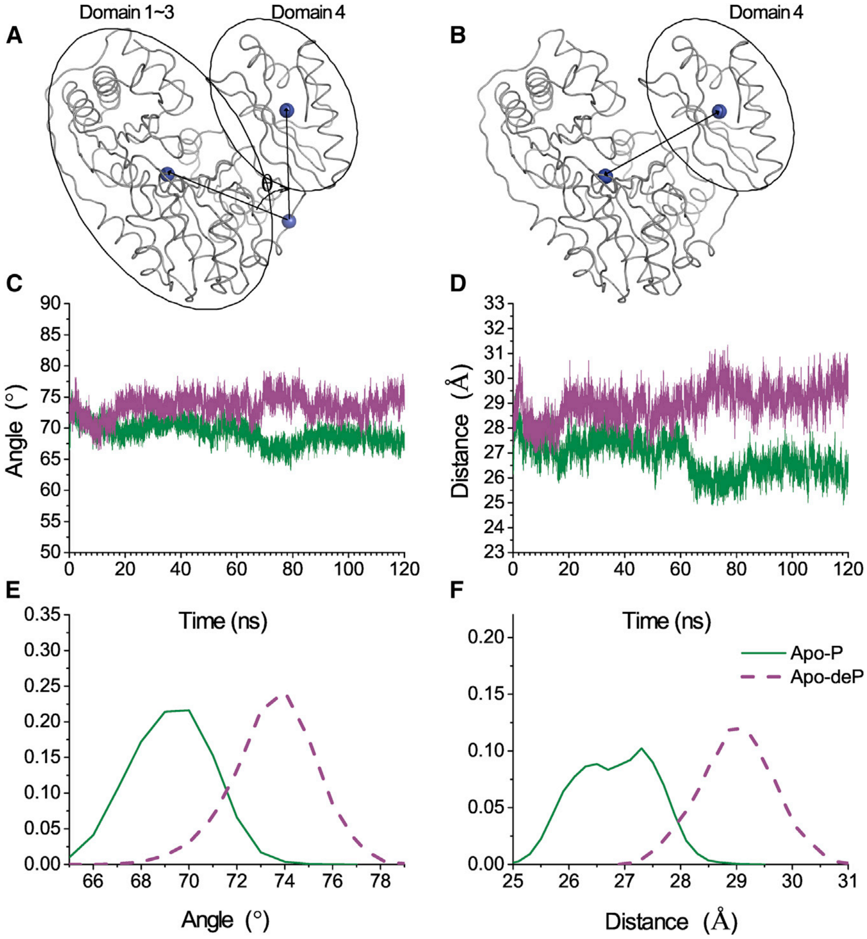

FIGURE 5 D4 opens wider in Apo-deP than in Apo-P in MD simulations. (*A*, *C*, and *E*) Angle (θ) between the centers of mass (spheres in *A*) of D1–D3 and D4. (*B*, *D*, and *F*) Distances between the center of mass of D4 and the metal site (spheres in *B*). (*C*) The instantaneous angle between the centers is plotted. (*D*) Plot showing the instantaneous separation between the centers of mass in panel *D*. (*E*) Histogram marking the frequency with which the angle occurs over the equilibrated portions of the MD trajectories from 5 to 120 ns. (*F*) Histogram plotting the frequency with which the separation occurs between 5 and 120 ns. Green represents the Apo-P simulation and purple represents Apo-deP. To see this figure in color, go online.

(Fig. 5 *A*) averaged 69.3° ± 1.7° (Fig. 5, *C* and *E*). In Apo-deP, this angle averaged 73.6 ± 1.7° (i.e., more than 4° wider). In Apo-P, the distances between the catalytic metal site and the center of mass of D4 (Fig. 5 *B*) averaged 26.8 ± 0.7 Å, with double maxima around 26.5 and 27.5 Å in the histogram and greater compaction after 60 ns (Fig. 5, *D* and *F*). The distance of separation in Apo-deP averaged 29 ± 0.7 Å (i.e., often more than 2 Å greater than that in Apo-P; Fig. 5, *D* and *F*). D4 of Apo-deP also manifested greater movement relative to D3 by an orthogonal mode not shown. The radius of gyration was also larger in Apo-deP (Fig. S10). Although the crystal structures of Apo-P and Apo-deP differ very little (19), the MD simulations imply that Apo-deP samples a wider range of conformations in solution than does Apo-P. We also reproduced the MD results for Apo-deP by starting with the Apo-P crystal structure, after removing its phosphoryl group and recalculating the surrounding partial charges. Further simulations of the S108E mutant (a partial phosphomimetic modeled from the Apo-deP coordinates of PDB 4MRQ) resulted in a compact form like that of Apo-P, although with a smaller angle of separation of D4 of 66–67°. The greater separation and freedom of D4 in Apo-deP simulations strongly support the hypothesis that phosphorylation of Ser-108 electrostatically attracts D4, limiting its mobility. This electrostatic compaction by phosphorylation may be called electrostriction, a behavior of dielectric materials that is well known in materials science and acknowledged in biomacromolecules (45).

Phosphorylation effects on simulated backbone mobility and HX

The backbone RMSFs in MD simulations of Apo-P and Apo-deP are generally similar (Fig. 6 *A*) but for the following exceptions: phosphorylation enhances the simulated backbone rigidity in D2 near phosphoSer-108, the core of D3, part of the D3 interface with D4, and the face of D4 toward the catalytic cleft and D3. Surprisingly, phosphorylation appears to subtly increase backbone mobility in parts of D1.

Previous studies have correlated HX protection factors with dynamics simulations via a linear combination of the fluctuating contacts with either H-bonds or RMSF^{-1} (23,24). Using three of the same proteins studied previously, we found that we could obtain improved correlations by

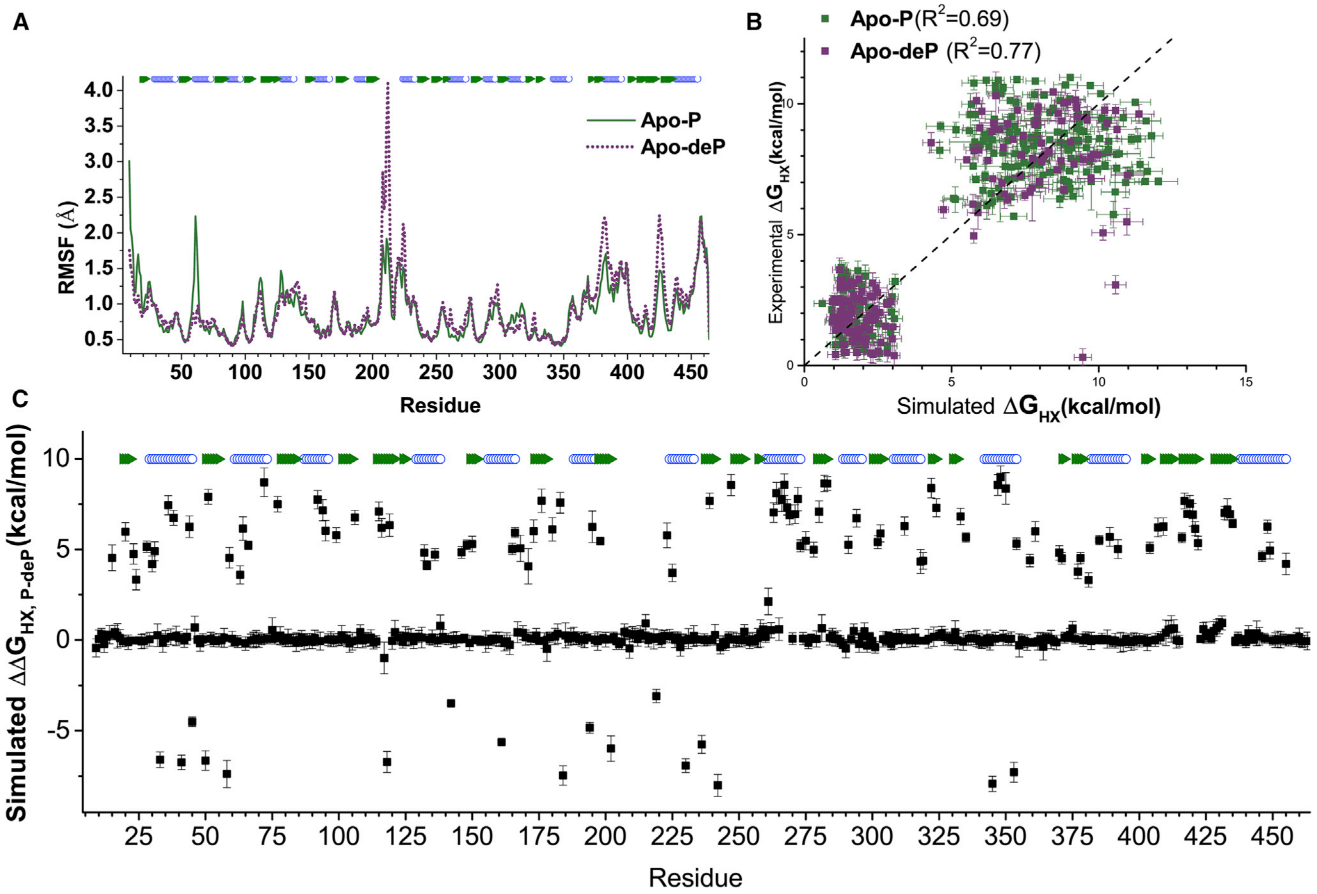

FIGURE 6 Simulated phosphorylation-dependent changes in free energies of HX, derived from the MD trajectories, agree with the locations of experimentally measured changes. (*A*) Backbone RMSFs of Apo-P and Apo-deP are compared. (*B*) Measured ΔG_{HX} is plotted against ΔG_{HX} simulated from each MD trajectory using $\ln(P_n^{sim})$ values simulated using Eq. 3 and the pairs of β_c and $\beta_{1/\mathrm{RMSF}}$ coefficients in the text and at the bottom of Table S4. (*C*) The differences in the simulated ΔG_{HX} modeled from the MD trajectories of Apo-P and Apo-deP are plotted against the sequence position for comparison with Fig. 3 *A*. To see this figure in color, go online.

optimizing and applying separate sets of coefficients of Eq. 3 for rapid and slow regimes of HX (Table S3), as shown by a comparison of the previous and new analyses of the HX data for staphylococcal nuclease (Fig. S11). We optimized the coefficients of Eq. 3 for the number of contacts N_n^c and RMSF^{-1} as described previously (24) for agreement with the HX rates of PMM/PGM across the 120 ns MD trajectories, but with the enhancement of two sets of coefficients. The coefficients obtained are $\beta_c = 0.22$ and $\beta_{1/\mathrm{RMSF}} = 0.28$ for the less protected amide groups. The coefficients are $\beta_c = 0.56$ and $\beta_{1/\mathrm{RMSF}} = 3.94$ for the more protected residues (Table S4). We used these coefficients to simulate the protection factors and free energies of HX from the MD trajectories for both the rapid and slow cases of HX (Fig. 6 *B*). Differences in these simulated free energies between the phosphorylated and dephosphorylated states are plotted in Fig. 6 *C*. Significant increases in $\ln(P_n^{sim})$ and ΔG_n^{sim} in Apo-P are based on increased contacts and H-bonding, and lower RMSFs at those sites in the MD trajectory (see Eq. 3 above). Although the magnitudes of the simulated large protection factors (free energies in the EX2 regime) obtained by this approach are not quantitatively reliable (23) (Fig. 6 *B*), the locations and patterns of protection and deprotection by phosphorylation (Fig. 6 *C*) are in a qualitative sense remarkably consistent with the locations measured to have a strong dependence of HX on phosphorylation status (Fig. 3 *A*). The simulated increases of $\Delta\Delta G_{HX,P\text{-}deP}$ identify more than 80% of the sites with measured increases (Figs. 3 *A* and 6 *C*), i.e., 85% of the amide groups with increased protection in D1, 87% in D2, 83% in D3, and 81% in D4. The simulated decreases identify all 14 residues in D1, D2, and D3, with $\Delta\Delta G_{HX,P\text{-}deP}$ being decreased by >2 kcal/mol (Figs. 3 *A* and 6 *C*). Thus, the differences between the MD trajectories of Apo-P and Apo-deP agree with the distribution of not only the HX slowed by phosphorylation (densest between D4 and D3) but also the phosphorylation-hastened HX in D1–D3.

DISCUSSION

The studies described herein reveal the extent of the increased rigidity of PMM/PGM due to phosphorylation, revising a recent qualitative assessment (19) with residue-specific and quantitative detail. The computational studies agree with the sites of phosphorylation-increased and -decreased protection from HX, and furnish strong evidence that the structural compaction is electrostatic in nature.

Structural compaction by phosphorylation

Dephosphorylation partially frees D4 in MD simulations, typically increasing its separation from the center of PMM/PGM by 1 Å to 4 Å (Fig. 5, *D* and *F*). This is consistent with the 1 Å larger radius of gyration of the dephosphorylated form suggested by small-angle x-ray scattering (19). Expansion of Apo-deP agrees with the increase of simulated backbone fluctuations at the D3-D4 interface (Fig. 6), faster HX at this interface, destabilization of D3 and two β-strands of D4 facing D3 (Fig. 3), and NMR line-broadening evidence of a conformational exchange in these regions (Fig. S3). The lack of expansion of Apo-deP in its crystal structure (19) was attributed to restriction of the crystal lattice. Without this constraint, all of the solution measurements and simulations agree with Apo-deP being loosened and expanded. The compaction of Apo-P may now be attributed to the electrostatic attraction of the positive face of D4 for phosphoSer-108 and adjoining electronegative surfaces of D2 (Fig. 4 *C*), i.e., electrostriction. The closer packing of D4 against D3 and superficially with D1 (Fig. 7 *B*) must result from this, accounting for the longer-lived H-bonds and enhanced stability in these regions.

Catalytic relevance of compaction by phosphorylation and loosening by dephosphorylation

The phosphoryl group at Ser-108 of PMM/PGM forms H-bonds with hydroxyl groups of substrates (17) and is transferred to and from the hexose phosphate substrates during catalysis (5,6) (Fig. 1). The evidence presented here suggests that the phosphoryl group also serves to narrow the catalytic cleft of the enzyme (Fig. 7). This may help position phosphoSer-108 and the substrate for H-bond formation and subsequent phosphoryl transfer to the 1- or 6-hydroxyl group of the substrate.

The unusual 180° rotation of G16P and mannose 1,6-bisphosphate intermediates, which occurs in the middle of the catalytic cycle during association with PMM/PGM (8), may also be facilitated by changes in the dynamics of the transiently dephosphorylated enzyme. Measurements of accessibility to probes (Fig. 2), HX (Figs. 3 and S6), radius of gyration (19), electrostatics (Fig. 4), and MD simulations (Figs. 5, 6, and 7) establish that Apo-deP has a wider catalytic cleft and is looser overall, except for small portions of D1 and D2 that may gain rigidity upon dephosphorylation (Figs. 3 and 6; Table S2). Expansion and opening of the cleft could help accommodate the catalytically required 180° reorientation of the bisphosphorylated intermediate.

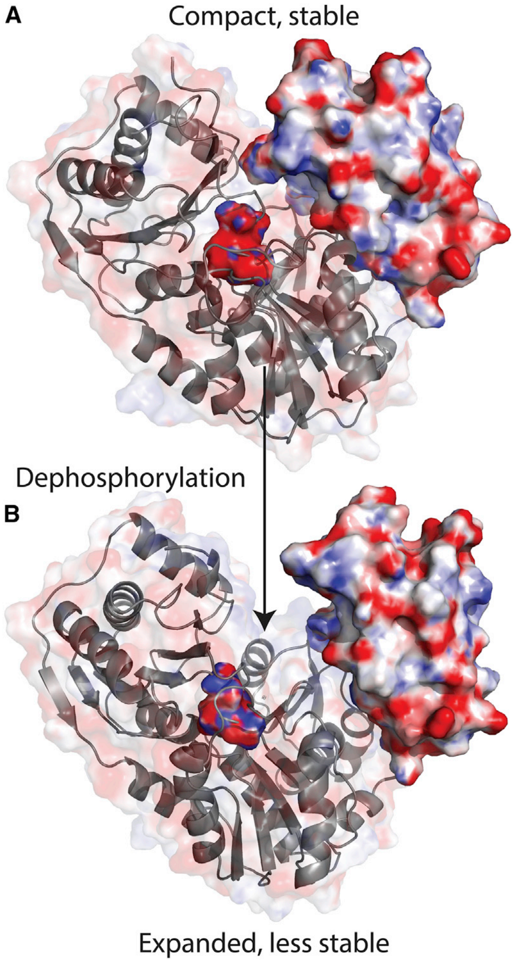

FIGURE 7 Expansion of PMM/PGM accompanying its dephosphorylation. The surfaces colored by electrostatics are plotted for D4 and around Ser-108 at the base of the cleft. (*A*) Phosphorylation of Ser-108 stabilizes the domains of PMM/PGM through electrostatic attraction of D4. Apo-P at 82 ns in the MD trajectory is plotted. (*B*) Transient dephosphorylation during the catalytic cycle appears to free D4 partially, resulting in an expanded structure with less rigidity in the D3–D4 region. Apo-deP at 117 ns in its MD trajectory is plotted. To see this figure in color, go online.

The stabilization of the active site of PMM/PGM by phosphorylation is less than that at distal sites (Fig. 3). Despite coordination of Mg^{2+} by three aspartate side chains in the active site, phosphorylation of Ser-108 nearby might introduce a degree of repulsion from these three carboxylate groups. This may account for the phospho-destabilization of Mg^{2+} ligand Asp-242, a few neighboring residues, and other residues in D2. Locally diminished stability near the active site due to phosphorylation required for enzyme activity could be reminiscent of observed trends of trade-offs between stability and function, in which clefts and their key residues for catalysis tend to destabilize the protein fold (46,47).

Insights into HX by NMR beyond qualitative HDX-MS

The NMR studies reveal that the HX behavior within PMM/PGM is more complex and varied than was previously appreciated. The most obvious trend of phosphorylation-increased rigidity and stability to HX is clearly long in range, with the distant core of D3 and proximal face of D4 being especially shielded by Ser-108 phosphorylation (Fig. 3). However, the residue-by-residue accounting provided by NMR also implicates ~99 residues with HX unaffected by phosphorylation and 24 residues with HX increased by phosphorylation (Fig. 3). This is corroborated by comparison with the changes in HX protection factors (free energies) simulated from the MD trajectories (Fig. 6 *C*). Among the 237 residues for which $\Delta\Delta G_{HX,P\text{-}deP}$ comparisons of HX are available, 48% represent significant slowing by phosphorylation, 10% undergo acceleration by phosphorylation, and 42% have little dependence on phosphorylation (Fig. 3 *A*). The computational results are consistent with this, but suggest that a much higher proportion of residues are unaffected by phosphorylation (Fig. 6 *C*). Thus, in light of the NMR and computational data, the HDX-MS-based proposal that flexibility increases of PMM/PGM upon dephosphorylation are global (19) should not be construed as universal or comprehensive. Six of the peptides monitored by HDX-MS are shown by NMR to have at least two residues each with increased HX upon Ser-108 phosphorylation (Table S2). Four more peptides have single residues accelerated in HX by NMR. Most of the regions with HX expedited by phosphorylation map to portions of D1 and D2, including Asp-242 at the active site (Figs. 3 and 6 *C*; Movie S1). Observation of the varying and nuanced HX behaviors, including local destabilizations within this multidomain enzyme, required the residue resolution and quantification of NMR (enhanced by subsecond and long timescales). The phosphorylation-induced changes in rigidity are long in range, with widespread increases and localized decreases in stability.

To our knowledge, the NMR methods have also provided the first detailed HX insight into functionally important loops within the active site of PMM/PGM, where HDX-MS did not contribute. For example, HDX by NMR identified the residues flanking Ser-108 in sequence as being stabilized by its phosphorylation (Fig. 3), whereas MS failed to detect the peptide containing Ser-108 when it was phosphorylated (92–117 in Table S2). Neighboring residues in D2 and D3 that were destabilized by phosphoSer-108 were already noted (Fig. 3). NMR also revealed key ligand-binding residues protected by phosphorylation in two other peptides: 1) the C-terminal half of HDX-MS peptide 14–27 (containing key Arg-20 at the active site); and 2) the middle third of peptide 407–429 near Arg-421 and Ser-423 that binds the phosphate group of ligands.

Using NMR, we were able to quantify the rates and thermodynamics of HX of specific amide groups, which allowed us to examine the stabilities of individual H-bonds, domains, and the enzyme as a whole. This revealed phosphorylation-dependent increases in stability that are locally large for individual H-bonds (>4 kcal/mol at many sites in D1, D3, and D4), moderate in the folding stability of D3 and D4 ($\geq$1.3 kcal/mol), and more subtle for the enzyme as a whole ($\geq$0.4 kcal/mol) (Figs. 3, S6, and S9). Along with localized variations in stability (Figs. 3 and 6; Movies S1 and S2), these findings provide a complex but unified biophysical portrayal. The combination of HX methods and dynamics simulations (Fig. 3 and 6) may have wider applicability for appreciating the varied effects of phosphorylation on proteins.

Long-range effects of phosphorylation on HDX of enzymes

Phosphorylation of Ser-108 slowed HDX to the farthest reaches of D2–D4 (Fig. 3). Moreover, the addition of two negative charges at the site of phosphorylation attracted D4 in both static and dynamic simulations, resulting in domain rotation about the flexible hinge between D3 and D4 (Figs. 5, 6, and 7). These results are reminiscent of those due to phosphorylation in other systems. For example, phosphorylation of the activation segment of p38 MAP kinase at two sites or protein kinase A (PKA) at a single site analogously slowed HDX of loops at long range and locally in the activation segment, and increased the folding stability of PKA (48,49). In the protein kinase ERK2, dual phosphorylation of the activation segment also induced long-range changes in HDX (mostly small decreases) as well as increases in four peptides, suggesting functionally relevant mobility in its ATP-binding loop and activation segment (50). The results for PMM/PGM suggest that the trend of phosphorylation restricting motions at long range while enabling some motions closer to the active site may be shared among some members of the protein kinase and α-D-phosphohexomutase superfamilies, which are mechanistically very different phosphoryl transfer enzymes. Mobility appears to modulate substrate access to protein kinases and the 180° reorientation of the intermediate in dephosphorylated PMM/PGM.

CONCLUSIONS

Our calculations strongly suggest that phosphorylation of Ser-108 in D1 electrostatically attracts D4, narrowing the catalytic cleft and breadth of PMM/PGM. This electrostriction accounts for the properties of the phosphorylated form (Apo-P) demonstrated above, i.e., less accessibility to probes, enhanced folding stability, stabilization of many H-bonds by >4 kcal/mol, much slowing of HX with stability increases of >1.3 kcal/mol for D3 and the adjacent face of D4, and increased rigidity in the stabilized D3-D4 interface. Narrowing of the active-site cleft due to phosphorylation probably aids capture of phosphohexose substrates, whereas opening upon dephosphorylation aids rotation of the bisphosphorylated intermediate. NMR and MD simulations paint a more complex, varied, and detailed landscape of HX changes than does peptide-resolved HDX-MS. The proposal that flexibility increases in the dephosphorylated form (Apo-deP) are global (19) must be tempered by the observation of a large number of unaffected sites and some sites with dephosphorylation-induced slowing of HX, especially in D1 and D2, which is also supported by MD trajectories. The rigidity increases upon phosphorylation are widespread, being mostly concentrated in D3 and D4, which draw closer upon phosphorylation. The ~100 sites with phosphorylation-promoted stability increases, as well as the stability decreases in D1 and D2, are truly long-range effects that reach the most distant flanks of the enzyme. Such behaviors parallel HDX-MS characterizations of protein kinases, suggesting analogous long-range effects of phosphorylation in both superfamilies of multidomain enzymes.

SUPPORTING MATERIAL

Supporting Materials and Methods, eleven figures, three equations, four tables, and two movies are available at http://www.biophysj.org/biophysj/supplemental/S0006-3495(14)04745-6.

ACKNOWLEDGMENTS

We thank A. Hopkins for enzyme preparations and S. Jiang for assistance with interleaving of the CLEANEX pulse sequence.

This work was supported by National Science Foundation grants MCB 0918389 and 1409898. National Institutes of Health grant S10RR022341 contributed to the purchase of the 800 MHz NMR spectrometer.

REFERENCES

1. Johnson, L. N., and R. J. Lewis. 2001. Structural basis for control by phosphorylation. *Chem. Rev.* 101:2209–2242.
2. Taylor, S. S., M. M. Keshwani, ..., A. P. Kornev. 2012. Evolution of the eukaryotic protein kinases as dynamic molecular switches. *Philos. Trans. R. Soc. Lond. B Biol. Sci.* 367:2517–2528.
3. Xin, F., and P. Radivojac. 2012. Post-translational modifications induce significant yet not extreme changes to protein structure. *Bioinformatics.* 28:2905–2913.
4. Johnson, L. N., and M. O'Reilly. 1996. Control by phosphorylation. *Curr. Opin. Struct. Biol.* 6:762–769.
5. Naught, L. E., and P. A. Tipton. 2001. Kinetic mechanism and pH dependence of the kinetic parameters of *Pseudomonas aeruginosa* phosphomannomutase/phosphoglucomutase. *Arch. Biochem. Biophys.* 396:111–118.
6. Regni, C., P. A. Tipton, and L. J. Beamer. 2002. Crystal structure of PMM/PGM: an enzyme in the biosynthetic pathway of *P. aeruginosa* virulence factors. *Structure.* 10:269–279.
7. Ray, Jr., W. J., and G. A. Roscelli. 1964. A kinetic study of the phosphoglucomutase pathway. *J. Biol. Chem.* 239:1228–1236.
8. Naught, L. E., and P. A. Tipton. 2005. Formation and reorientation of glucose 1,6-bisphosphate in the PMM/PGM reaction: transient-state kinetic studies. *Biochemistry.* 44:6831–6836.
9. Regni, C., A. M. Schramm, and L. J. Beamer. 2006. The reaction of phosphohexomutase from Pseudomonas aeruginosa: structural insights into a simple processive enzyme. *J. Biol. Chem.* 281:15564–15571.
10. Ballok, A. E., and G. A. O'Toole. 2013. Pouring salt on a wound: Pseudomonas aeruginosa virulence factors alter Na^+ and Cl^- flux in the lung. *J. Bacteriol.* 195:4013–4019.
11. Li, X. J., Q. Li, ..., Q. Y. Yuan. 2011. Bacteriological differences between patients with acute exacerbation of COPD and community-acquired pneumonia. *Respir. Care.* 56:1818–1824.
12. Govan, J. R. W., and V. Deretic. 1996. Microbial pathogenesis in cystic fibrosis: mucoid *Pseudomonas aeruginosa* and *Burkholderia cepacia*. *Microbiol. Rev.* 60:539–574.
13. Ye, R. W., N. A. Zielinski, and A. M. Chakrabarty. 1994. Purification and characterization of phosphomannomutase/phosphoglucomutase from Pseudomonas aeruginosa involved in biosynthesis of both alginate and lipopolysaccharide. *J. Bacteriol.* 176:4851–4857.
14. King, J. D., D. Kocíncová, ..., J. S. Lam. 2009. Review: lipopolysaccharide biosynthesis in Pseudomonas aeruginosa. *Innate Immun.* 15:261–312.
15. Olvera, C., J. B. Goldberg, ..., G. Soberón-Chávez. 1999. The Pseudomonas aeruginosa algC gene product participates in rhamnolipid biosynthesis. *FEMS Microbiol. Lett.* 179:85–90.
16. Remminghorst, U., and B. H. Rehm. 2006. Bacterial alginates: from biosynthesis to applications. *Biotechnol. Lett.* 28:1701–1712.
17. Regni, C., L. Naught, ..., L. J. Beamer. 2004. Structural basis of diverse substrate recognition by the enzyme PMM/PGM from *P. aeruginosa*. *Structure.* 12:55–63.
18. Sarma, A. V., A. Anbanandam, ..., S. R. Van Doren. 2012. Solution NMR of a 463-residue phosphohexomutase: domain 4 mobility, substates, and phosphoryl transfer defect. *Biochemistry.* 51:807–819.
19. Lee, Y., M. T. Villar, ..., L. J. Beamer. 2014. Promotion of enzyme flexibility by dephosphorylation and coupling to the catalytic mechanism of a phosphohexomutase. *J. Biol. Chem.* 289:4674–4682.
20. Coales, S. J., S. Y. E, ..., Y. Hamuro. 2010. Expansion of time window for mass spectrometric measurement of amide hydrogen/deuterium exchange reactions. *Rapid Commun. Mass Spectrom.* 24:3585–3592.
21. Mayne, L., Z.-Y. Kan, ..., S. W. Englander. 2011. Many overlapping peptides for protein hydrogen exchange experiments by the fragment separation-mass spectrometry method. *J. Am. Soc. Mass Spectrom.* 22:1898–1905.
22. Huyghues-Despointes, B. M., J. M. Scholtz, and C. N. Pace. 1999. Protein conformational stabilities can be determined from hydrogen exchange rates. *Nat. Struct. Biol.* 6:910–912.
23. Vendruscolo, M., E. Paci, ..., M. Karplus. 2003. Rare fluctuations of native proteins sampled by equilibrium hydrogen exchange. *J. Am. Chem. Soc.* 125:15686–15687.
24. Kieseritzky, G., G. Morra, and E.-W. Knapp. 2006. Stability and fluctuations of amide hydrogen bonds in a bacterial cytochrome c: a molecular dynamics study. *J. Biol. Inorg. Chem.* 11:26–40.
25. Cellini, B., R. Montioli, ..., C. B. Voltattorni. 2010. Molecular defects of the glycine 41 variants of alanine glyoxylate aminotransferase associated with primary hyperoxaluria type I. *Proc. Natl. Acad. Sci. USA.* 107:2896–2901.
26. Lescop, E., P. Schanda, and B. Brutscher. 2007. A set of BEST triple-resonance experiments for time-optimized protein resonance assignment. *J. Magn. Reson.* 187:163–169.

27. Delaglio, F., S. Grzesiek, …, A. Bax. 1995. NMRPipe: a multidimensional spectral processing system based on UNIX pipes. *J. Biomol. NMR.* 6:277–293.
28. Goddard, T. D., and D. G. Kneller. 2000. SPARKY. University of California, San Francisco, San Francisco.
29. Hwang, T. L., P. C. van Zijl, and S. Mori. 1998. Accurate quantitation of water-amide proton exchange rates using the phase-modulated CLEAN chemical EXchange (CLEANEX-PM) approach with a Fast-HSQC (FHSQC) detection scheme. *J. Biomol. NMR.* 11:221–226.
30. Hernández, G., and D. M. LeMaster. 2003. Relaxation compensation in chemical exchange measurements for the quantitation of amide hydrogen exchange in larger proteins. *Magn. Reson. Chem.* 41:699–702.
31. Bertini, I., K. Ghosh, …, P. R. Vasos. 2003. A high-resolution NMR study of long-lived water molecules in both oxidation states of a minimal cytochrome c. *Biochemistry.* 42:3457–3463.
32. Peters, M. B., Y. Yang, …, K. M. Merz, Jr. 2010. Structural survey of zinc containing proteins and the development of the zinc AMBER force field (ZAFF). *J. Chem. Theory Comput.* 6:2935–2947.
33. Frisch, M. J., G. W. Trucks, …, D. J. Fox. 2009. Gaussian 09, revision B.01. Gaussian, Inc., Wallingford, CT.
34. Hornak, V., R. Abel, …, C. Simmerling. 2006. Comparison of multiple Amber force fields and development of improved protein backbone parameters. *Proteins.* 65:712–725.
35. Baker, N. A., D. Sept, …, J. A. McCammon. 2001. Electrostatics of nanosystems: application to microtubules and the ribosome. *Proc. Natl. Acad. Sci. USA.* 98:10037–10041.
36. Humphrey, W., A. Dalke, and K. Schulten. 1996. VMD: visual molecular dynamics. *J. Mol. Graph.* 14:33–38, 27–38.
37. Yamasaki, K., T. Daiho, …, H. Suzuki. 2013. Roles of long-range electrostatic domain interactions and K+ in phosphoenzyme transition of Ca^{2+}-ATPase. *J. Biol. Chem.* 288:20646–20657.
38. Craddock, T. J., J. A. Tuszynski, and S. Hameroff. 2012. Cytoskeletal signaling: is memory encoded in microtubule lattices by CaMKII phosphorylation? *PLOS Comput. Biol.* 8:e1002421.
39. Schonbrunn, E., S. Eschenburg, …, N. Amrhein. 2000. Structural basis for the interaction of the fluorescence probe 8-anilino-1-naphthalene sulfonate (ANS) with the antibiotic target MurA. *Proc. Natl. Acad. Sci. USA.* 97:6345–6349.
40. Bai, Y., T. R. Sosnick, …, S. W. Englander. 1995. Protein folding intermediates: native-state hydrogen exchange. *Science.* 269:192–197.
41. Linderstrøm-Lang, K. 1955. Deuterium exchange between peptides and water. *Chem. Soc. (Lond.). Spec. Publ.* 2:1–20.
42. Yan, S., S. D. Kennedy, and S. Koide. 2002. Thermodynamic and kinetic exploration of the energy landscape of Borrelia burgdorferi OspA by native-state hydrogen exchange. *J. Mol. Biol.* 323:363–375.
43. Liang, X., G. I. Lee, and S. R. Van Doren. 2006. Partially unfolded forms and non-two-state folding of a beta-sandwich: FHA domain from Arabidopsis receptor kinase-associated protein phosphatase. *J. Mol. Biol.* 364:225–240.
44. Huyghues-Despointes, B. M., U. Langhorst, …, J. M. Scholtz. 1999. Hydrogen-exchange stabilities of RNase T1 and variants with buried and solvent-exposed Ala —> Gly mutations in the helix. *Biochemistry.* 38:16481–16490.
45. Marky, L. A., and D. W. Kupke. 2000. Enthalpy-entropy compensations in nucleic acids: contribution of electrostriction and structural hydration. *Methods Enzymol.* 2000:419–441.
46. Beadle, B. M., and B. K. Shoichet. 2002. Structural bases of stability-function tradeoffs in enzymes. *J. Mol. Biol.* 321:285–296.
47. Liang, X., A. Arunima, …, S. R. Van Doren. 2010. Apparent tradeoff of higher activity in MMP-12 for enhanced stability and flexibility in MMP-3. *Biophys. J.* 99:273–283.
48. Sours, K. M., S. C. Kwok, …, N. G. Ahn. 2008. Hydrogen-exchange mass spectrometry reveals activation-induced changes in the conformational mobility of p38α MAP kinase. *J. Mol. Biol.* 379:1075–1093.
49. Steichen, J. M., G. H. Iyer, …, S. S. Taylor. 2010. Global consequences of activation loop phosphorylation on protein kinase A. *J. Biol. Chem.* 285:3825–3832.
50. Hoofnagle, A. N., K. A. Resing, …, N. G. Ahn. 2001. Changes in protein conformational mobility upon activation of extracellular regulated protein kinase-2 as detected by hydrogen exchange. *Proc. Natl. Acad. Sci. USA.* 98:956–961.

Supporting Material for:

Phosphorylation in the Catalytic Cleft Stabilizes and Attracts Domains of a Phosphohexomutase

Jia Xu, Yingying Lee, Lesa J. Beamer, and Steven R. Van Doren
Biochemistry Dept., 117 Schweitzer Hall, Univ. of Missouri, Columbia, MO 65211 USA

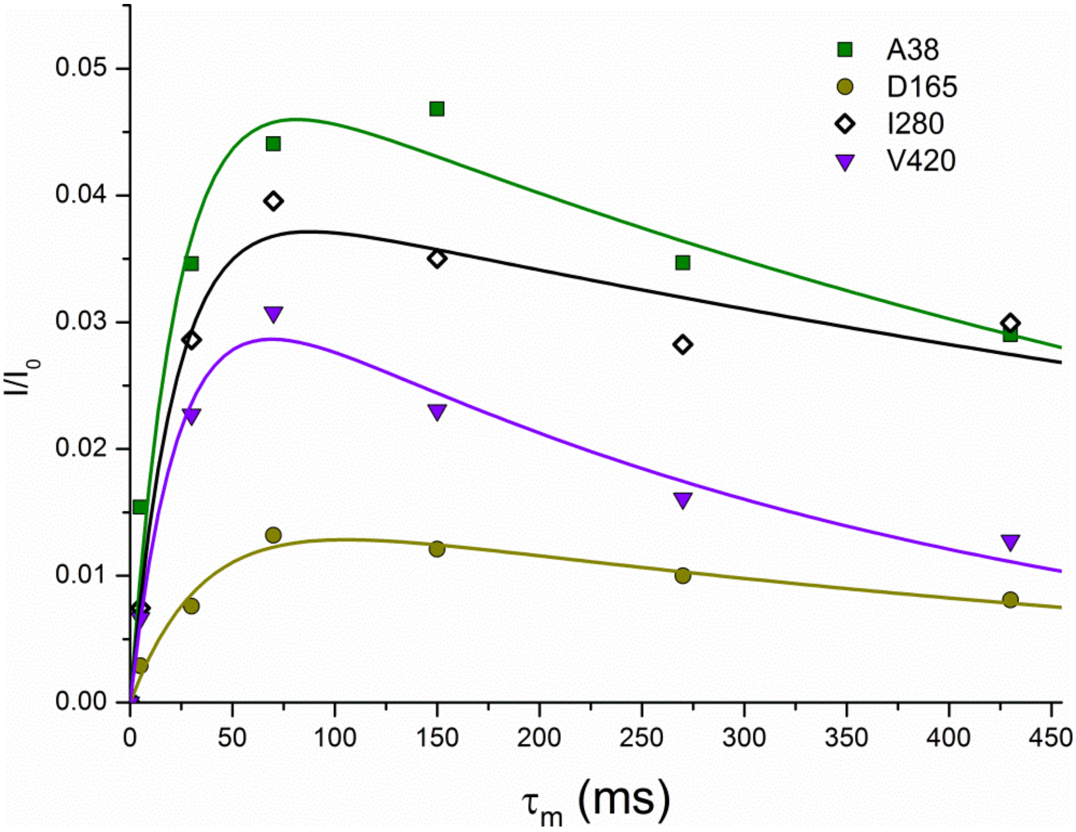

Figure S1. Examples of CLEANEX-PM time courses for the Apo-deP form of PMM/PGM. The fitted rate constants, k_{ex}, of Ala38, Asp165, Ile280, and Val420 are 2.8 ± 0.8 s^{-1}, 0.5 ± 0.1 s^{-1}, 1.9 ± 0.3 s^{-1}, and 1.1 ± 0.2 s^{-1}, respectively. These rate constants were used to simulate sub-second components of hydrogen exchange in the inset of Fig. 2D. The spin-lock during the mixing period used a radiofrequency field strength of 6.25 kHz. To maintain sample conditions consistent among the spectra during acquisition, the CLEANEX spectra were acquired in an interleaved manner and stored as a pseudo 3D spectrum. The interleaved pulse sequence and script developed to acquire and process the spectra are available as other Supplemental files.

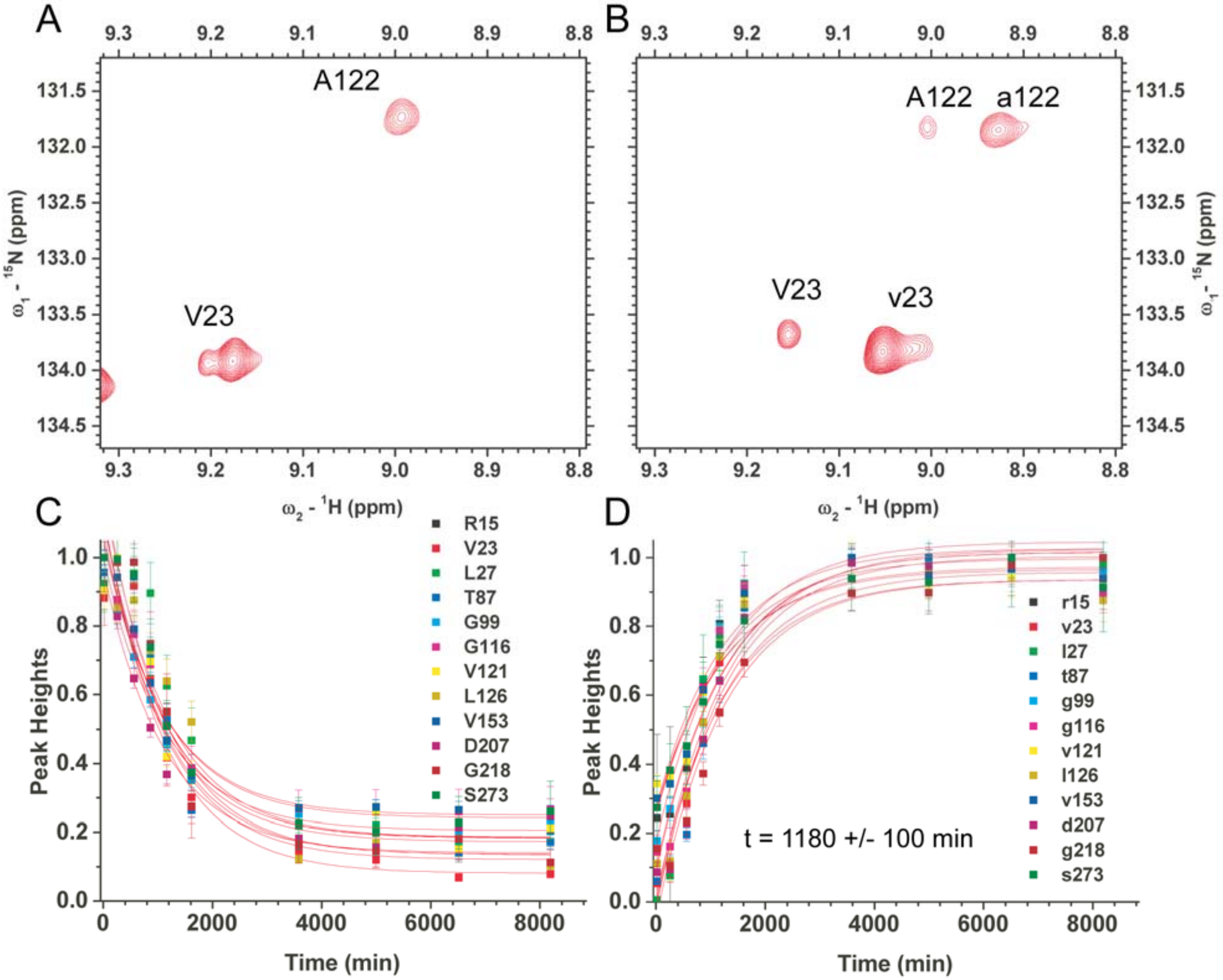

Figure S2. Kinetics of the apo-P form of PMM/PGM undergoing dephosphorylation. (A) Peaks of Val23 and Arg122 of Apo-deP 15 min after preparation are shown. (B) Peaks of the same sample after 60 h of dephosphorylation are shown. (C) The time course of the disappearance of 12 twelve normalized peaks representing the phosphorylated form is plotted. (D) The time course of the appearance of the peaks of the dephosphorylated form is plotted for the same 12 residues. These 12 used for illustration are a subset of the 43 actually used in global fits of the dephosphorylation kinetics that yielded a time constant of 1140 ± 70 min or 19.0 ± 1.1 h (where the uncertainty quoted is four-fold the fitting uncertainty).The TROSY NMR spectra were acquired at 35 °C, pH 7.5, 10 mM DTT, and 800 MHz.

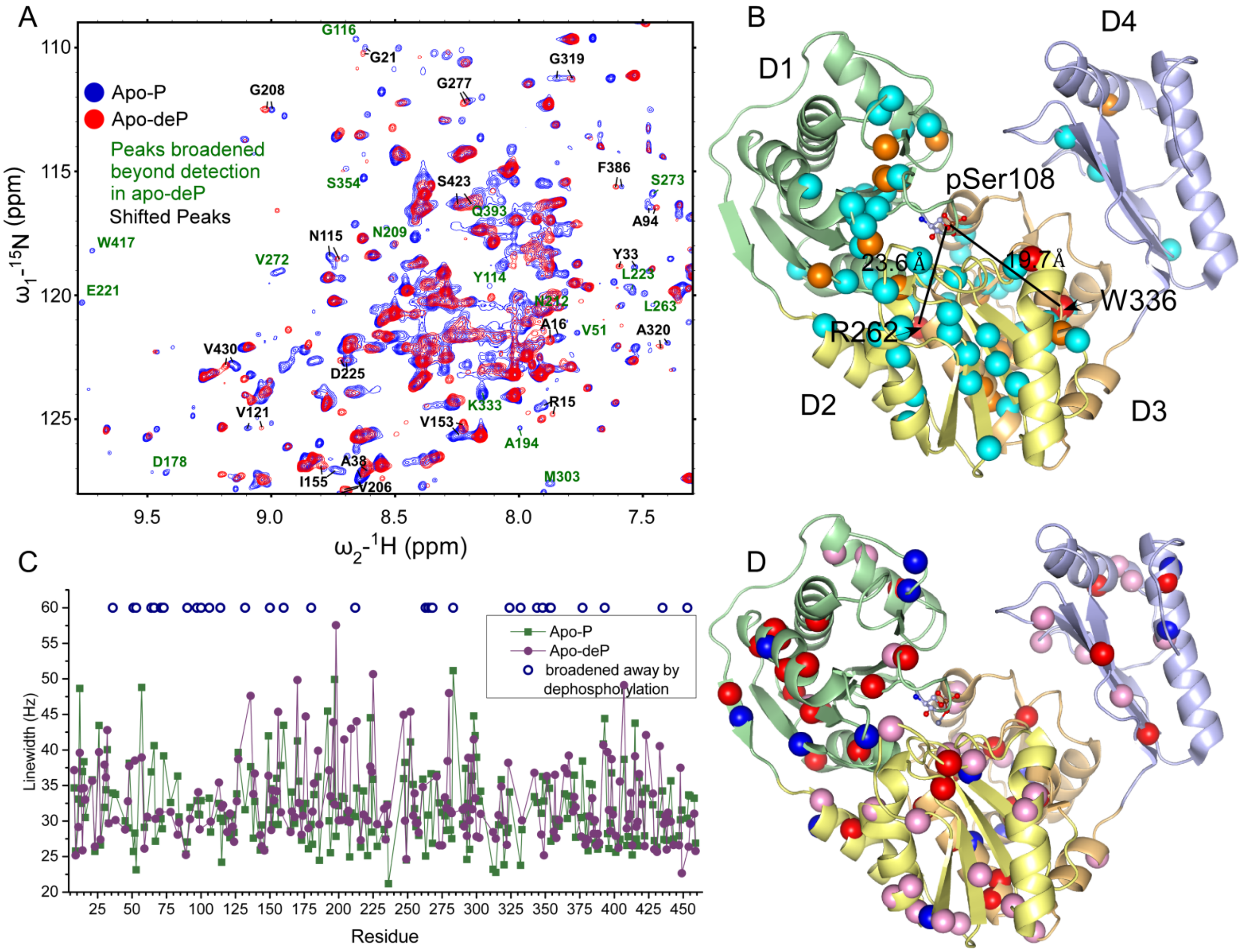

Figure S3. Effects of (de)phosphorylation on NMR spectra of PMM/PGM. (A) ^{15}N TROSY spectra of phosphorylated PMM/PGM (Apo-P; blue contours) and dephosphorylated PMM/PGM (Apo-deP; red) are superimposed. Dephosphorylation broadened beyond detection the peaks with green labels. The greater number of peaks of Apo-P reflects their being sharper and more readily detected. Conditions were 1 mM enzyme, pH 7.4, 308 K, and 800 MHz. (B) Locations of chemical shift perturbations introduced by dephosphorylation are marked on the crystal structure of Apo-P (PDB: 1K35) with red spheres for $\Delta\omega_{HN} > 0.2$ ppm, orange for $\Delta\omega_{HN} > 0.1$ ppm, and cyan for $\Delta\omega_{HN} > 0.03$ ppm, where $\Delta\omega_{HN} = ((\Delta\omega_H)^2 + (\Delta\omega_N/5)^2)^{1/2}$. The locations of Arg262 and Trp336 with the peaks most shifted by dephosphorylation are labeled along with their distances from pSer108. (C) Peaks broadened away by dephosphorylation are marked by open circles at top. The line widths plotted are each a composite of ^{1}H and ^{15}N line widths at half-height: $((\Delta v_{1/2,H})^2 + (\Delta v_{1/2,N})^2)^{1/2}$. (D) Amide peak broadenings by dephosphorylation are mapped on the structure in red where broadened away and pink where broadened > 20%, whereas blue marks amide peaks > 20% sharper in Apo-deP.

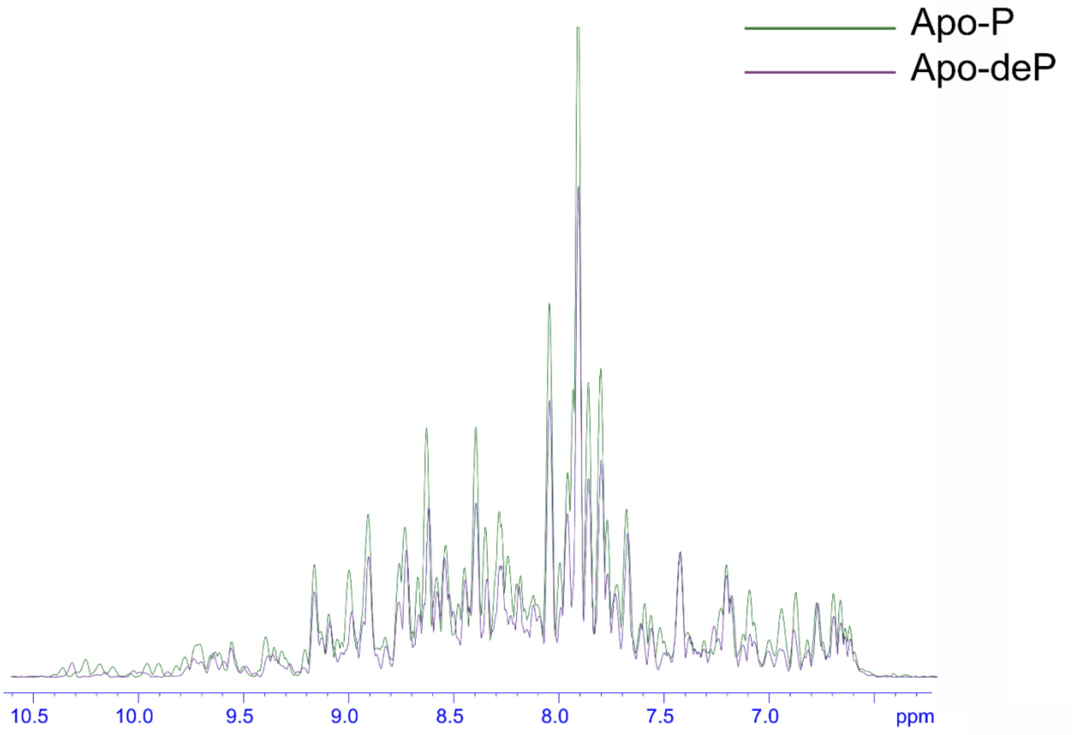

Figure S4. Skyline projections of 2D TROSY spectra of Apo-P before (green) and after more than 3 days at 35 °C where it has undergone dephosphorylation to apo-deP (purple).

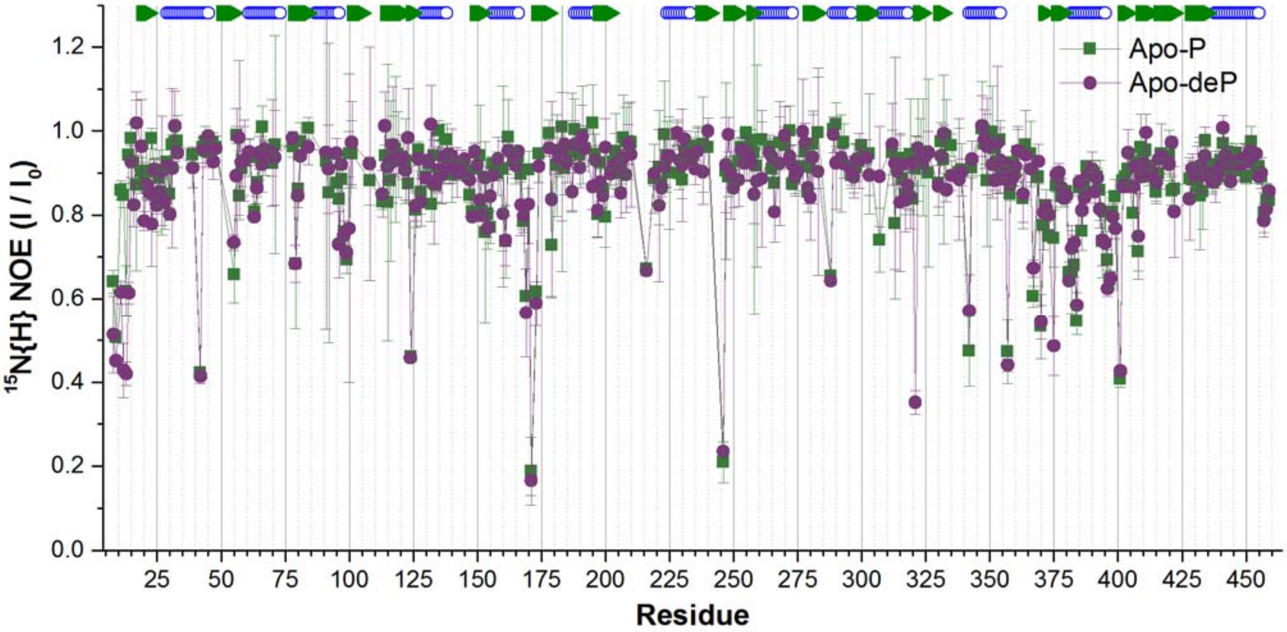

Figure S5. Dependence of ^{15}N{^{1}H} heteronuclear, steady-state NOE on phosphorylation status of PMM/PGM. Peak height with ^{1}H signal saturated is designated I and without saturation as I_0. The measurements were performed in triplicate at 800 MHz and 35 °C. The values plotted are mean ± SD (n= 3) for Apo-P in purple circles and Apo-deP in green squares. The locations of β-strands are marked with green arrows and helices with blue circles.

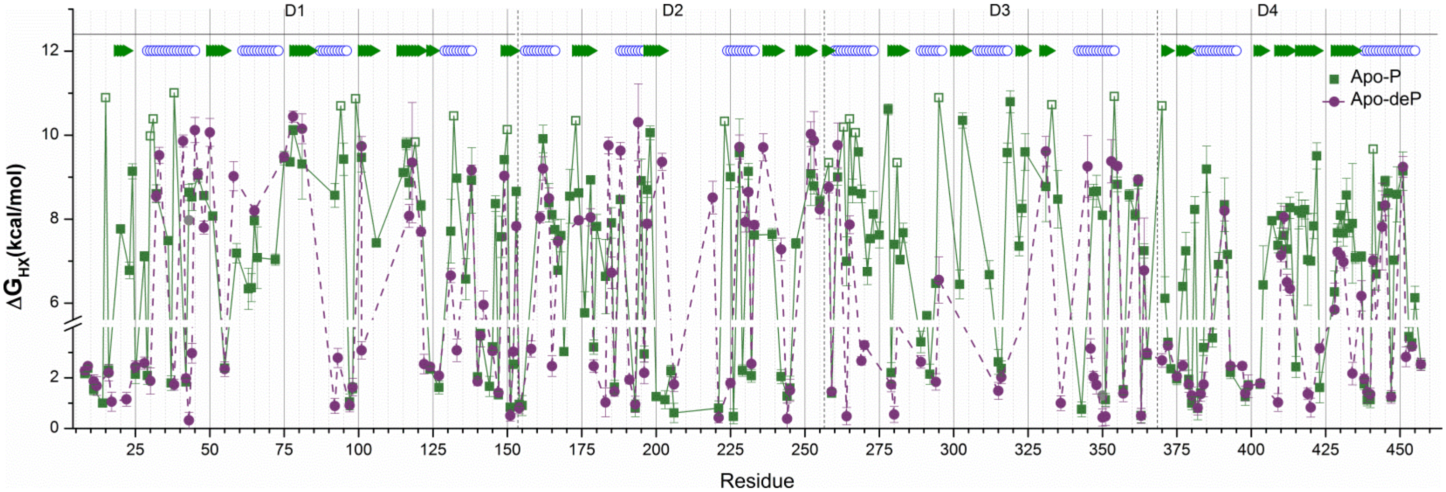

Figure S6. Phosphorylation slows HX and stabilizes domain 3 in particular. ΔG_{HX} values from slow HDX appear above the vertical break, while the small ΔG_{HX} values of rapid HX, measured on the sub-sec scale by CLEANEX-PM NMR (1), appear below the break. Open squares represent lower bounds of the ΔG_{HX} estimates for the especially slowly exchanging amide groups of Apo-P. The locations of strands and helices are marked at the top by triangles and blue circles, respectively.

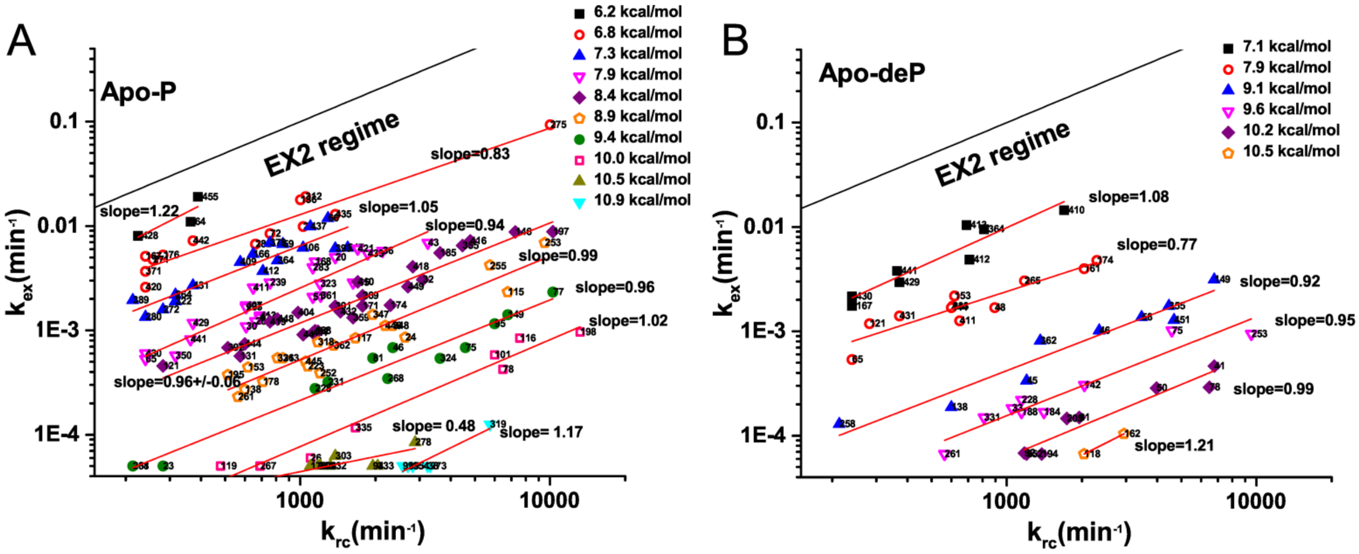

Figure S7. Hydrogen exchange results grouped by $\Delta G_{HDX,apparent}$ suggest the independence of $\Delta G_{HDX,apparent}$ from size of k_{rc}, implying that the EX2 regime prevails for both Apo-P (A) and Apo-deP (B). The reference line depicts the slope of 1.0 typifying the theoretical behavior of the EX2 regime. EX1 has a slope of zero. Residue numbers are listed by each point.

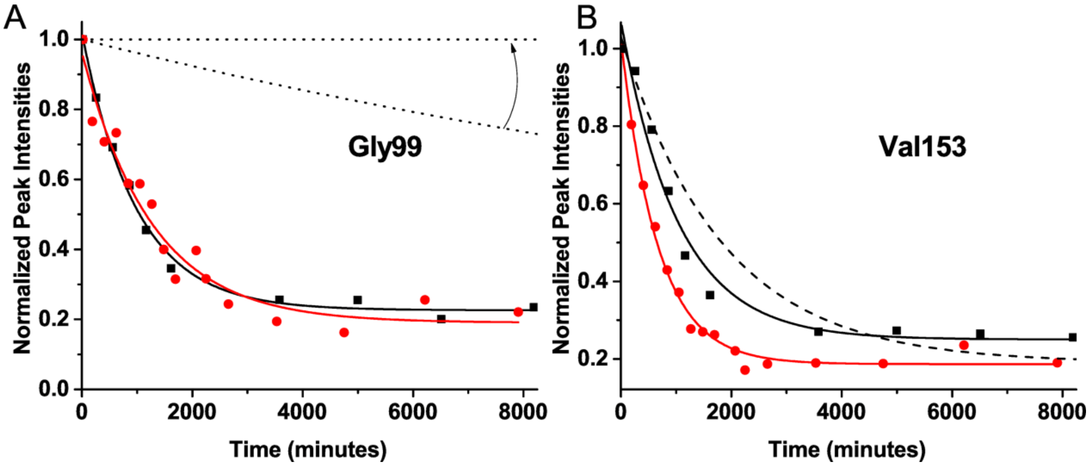

Figure S8. Examples of data fitting of apo-P. Since Apo-P undergoes dephosphorylation, its k_{ex} of HDX is calculated as $k_{ex}=k_{obs}- k_{deP}$. Black squares plot the apparent deuterium exchange curve in D_2O, providing k_{obs}. Red circles plot the decay of the peak in H_2O due to dephosphorylation, providing k_{deP}. Dashed lines mark the computed curve for k_{ex} from which effects of dephosphorylation are removed. (A) In the case of Gly99, the similarity of the two measured decays implies that k_{ex} approaches zero. The upper limit upon its k_{ex} is represented by the lower dashed line. Yet this cannot be experimentally distinguished from $k_{ex} = 0$ represented by the horizontal line, delimiting the other end of the range of potential k_{ex} values. (B) A simple case is illustrated for Val153 where $k_{ex} = k_{obs} – k_{deP}$.

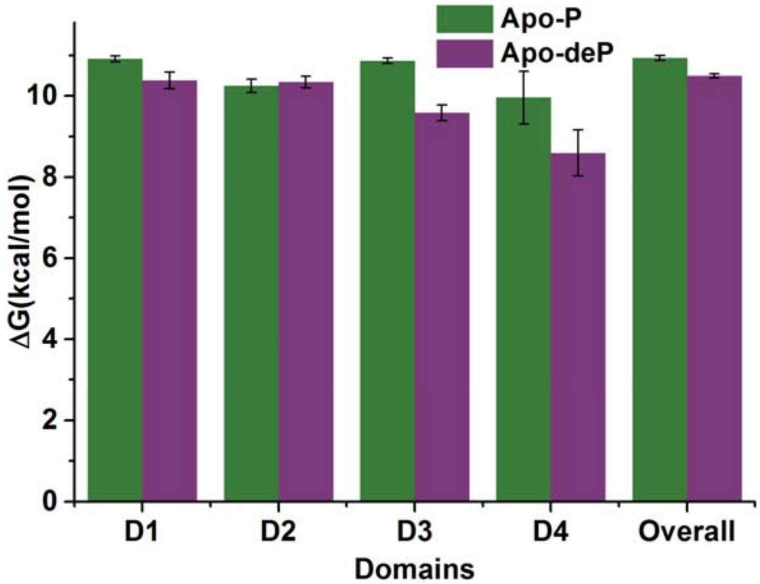

Figure S9. Phosphorylation slows HDX and stabilizes D3 and D4. The three highest ΔG_{HDX} values of each domain, or the enzyme as a whole, suggest the folding stability of that domain and its standard deviation by the method of ref (2) employed. The folding stabilities of Apo-P have been corrected for proline isomerization according to the method (2). The stabilities of Apo-P and its domains 1, 3, and 4 should be regarded as lower limits because the true size of their largest k_{ex} values (used for these ΔG_{fold} estimates) is masked by the rate of dephosphorylation.

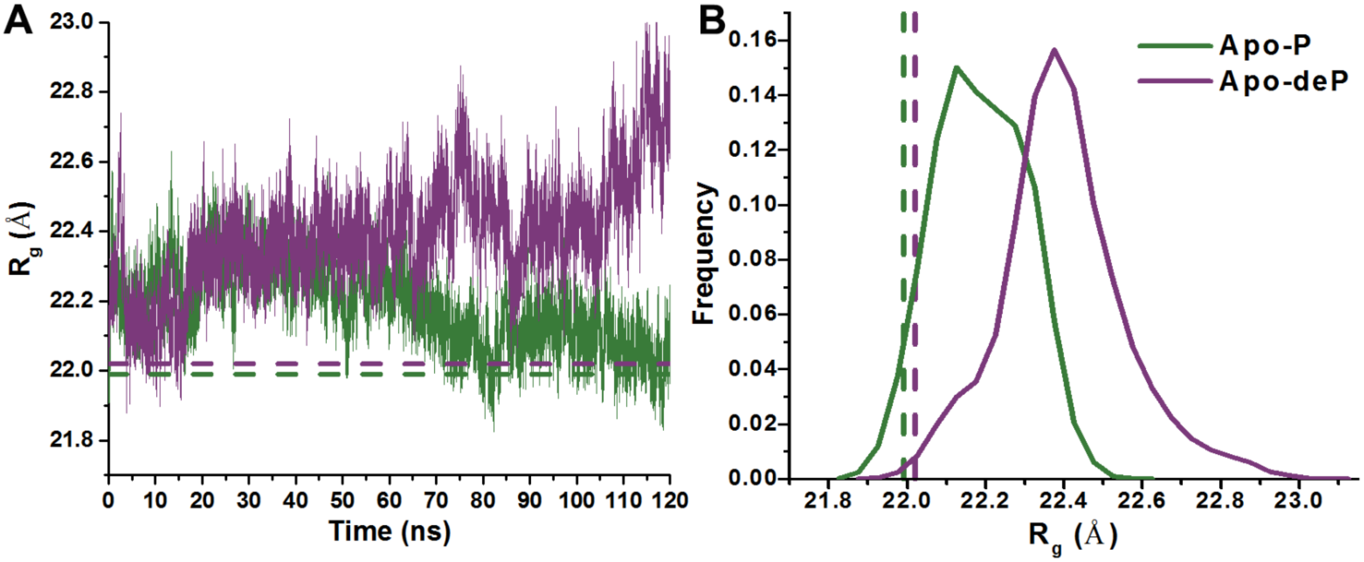

Figure S10. Radii of gyration (*R_g*) during MD trajectories indicate that the Apo-deP state (purple) is more expanded than Apo-P (green). Dashed lines represent the radii of the crystal structures of Apo-deP and Apo-P (PDB codes 4MRQ and 1K35, respectively). Panel (A) plots the time courses of *R_g* in the MD trajectories and (B) the histogram of *R_g* in the trajectories.

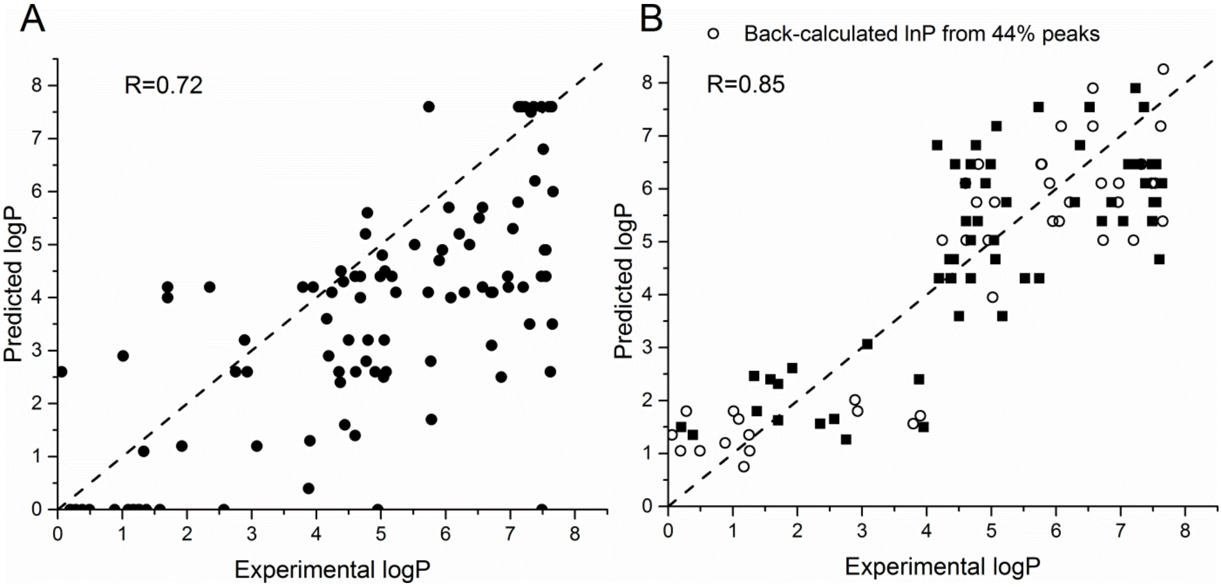

Figure S11. Correlation of experimentally measured HX protection factors *$ln(P^{exp})$* of staphylococcal nuclease with those simulated from its coordinates using (A) a single set of β_C and β_H coefficients as reported (3) or (B) two sets of coefficients optimized for rapid and slow regimes of HX using 44% of its residues (black squares); see eq. 3. The correlation is effective for the randomly chosen 31% of its residues not used in the optimization (open circles). (The other 25% of residues were not detected). Use of the two sets of coefficients (B) clearly improves the correlation of *$ln(P^{sim})$* compared with use of a single pair of coefficients (A); see Table S3.

SUPPORTING METHODS

^{15}N{^{1}H} NOE

^{15}N{^{1}H} steady-state NOE relaxation was measured with a Bruker Avance III 800 MHz NMR spectrometer using a pulse sequence with TROSY-enhanced ^{1}H resolution and sensitivity (4). In order to measure the protein under identical conditions, saturated and unsaturated ^{15}N{^{1}H} NOE spectra were collected in an interleaved manner. Each of the triplicate measurements of pairs of spectra of Apo-P was performed on freshly phosphorylated enzyme within 14 h of the phosphorylation. The triplicate measurements of spectra of Apo-deP were performed on freshly dephosphorylated enzyme in 17 h each. All samples were protected from oxidation with 10 mM DTT, Ar, and sealing with Shigemi tube plunger and parafilm.

Correction of HDX decays for lingering solvent

Since the HDX series were initiated by 5-fold dilution with D_2O-based buffer, 20% of solvent was still $^{1}H_2O$. The initial mixture decays as: $A(t) = A_0 \exp(-k_{obs} \times t) + A_\infty$, where the eventual peak size $A_\infty = 0.2 \cdot A_0$ reflects the original H_2O still present at 20%. The ~20 min dead time for sample handling, t_d, delayed acquisition of the first BEST-TROSY spectrum. The exponential decay following the dead time was fitted as:

$$A(t') = A'_0 \exp(-k_{obs} \times t') + A'_\infty \qquad \text{(eq. S1)}$$

where $A'_0 = A(t_d) = A_0 \exp(-k_{obs} \times t_d) + A_\infty$ and A'_∞ required fitting for each decaying peak because:

$$A'_\infty = \frac{A_\infty}{A_0 \exp(-k_{obs} \times t_d) + A_\infty} > 0.2 \times A'_0$$

A'_∞ exceeding 20% of A'_0 is evident in Fig. 2D.

Rate of dephosphorylation and correction of affected rates of HDX

In order to monitor the longevity of the phosphorylated form PMM/PGM and quantify the loss of its phosphorylation as the rate constant k_{deP}, control NMR experiments were set up in H_2O and acquired very similarly to those in D_2O. Decay rates in H_2O solvent were obtained by fitting a single exponential decay rate k_{deP} to the peak heights (Figs. 2D and S2C). Fitting peak heights and volumes gave equivalent results using eq. 2. However, 12 peaks of Apo-P and 10 peaks of Apo-deP underwent small, scattered shifts of the peak centers that introduced modest scatter to the decays; this was rectified using manual picking and volume integration of these peaks. Uncertainties were estimated from spectral noise and fitting errors. Global fitting of the decays of 43 peaks characteristic of Apo-P together with the concurrent increases of the peaks of Apo-deP of the same 43 residues, measured in spectra in H_2O (Fig. S2, C and D), provided the most reliable estimate of k_{deP}.

The rate constants of HDX (k_{ex}) of Apo-P form were corrected for its dephosphorylation by subtracting apparent k_{deP} from the observed rate constant of overall decay after dilution into D_2O: $k_{ex} = k_{obs} - k_{deP}$ (Fig. S8). For 98 Apo-P peaks without overlap with their counterparts of Apo-deP, each peak was corrected by its apparent k_{deP} values fitted independently to the decay of the corresponding peak measured in H_2O spectra. Most of the individually measured decays from dephosphorylation conform to the shared time constant of 19 h for dephosphorylation (Fig.

S2, C and D). However, 14 peaks were subject to an additional faster decay process in H_2O with a time constant of ~4.5 h which we fitted independently to generate pseudo k_{deP} values for use in correcting k_{ex}. Consequently, the decay rates of each individual peak in H_2O spectra were used in correcting the k_{obs} values in D_2O to the k_{ex} of HDX for the 98 amide peaks of Apo-P in the first two categories listed in Table S1. The globally fitted best estimate of k_{deP} was used to correct the k_{ex} of 44 peaks characteristic of Apo-P but overlapped with the corresponding peaks of Apo-deP, which are listed in the third and fourth categories in Table S1.

The k_{ex} rate constants of some well-protected residues appear to be nearly zero (Fig. S8A and S6, open squares). Therefore, upper bounds on k_{ex} were estimated in these most-protected cases. The smallest k_{obs} fitted to HDX spectra was 5.56 x 10^{-5} min^{-1}, suggesting that the slowest k_{ex} in the enzyme should be less than 5.56 x 10^{-5} min^{-1}.

In the HDX experiments, 13 residues with overlapped Apo-P and Apo-deP peaks in the TROSY spectra displayed k_{ex} unaffected by phosphorylation. *No correction* for rate of dephosphorylation was needed for these (fifth category of Table S1), as justified in the following section deriving behaviors possible with overlapped peaks.

Fitting of HDX decays of Apo-P peaks where overlapping Apo-deP peaks could develop during the time course

It can be demonstrated that the HDX decays of the overlapped NMR peaks of the phosphorylated and dephosphorylated enzyme forms can be described by this expression encompassing a wide range of scenarios:

$$Pe^{-(k_{ex,P}+k_{deP})t} + Qe^{-k_{ex,deP}t} \qquad \text{(eq. S2)}$$

where $P = \frac{a(k_{ex,P}-k_{ex,deP})}{k_{ex,P}-k_{ex,deP}+k_{deP}}$ and $Q = \frac{(1-a)(k_{ex,P}-k_{ex,deP})+k_{deP}}{k_{ex,P}-k_{ex,deP}+k_{deP}}$,

where *a* is the fraction of the enzyme in the phoshorylated state Apo-P, $k_{ex,P}$ is the rate constant of H(D)X of Apo-P, $k_{ex,deP}$ the rate constant of H(D)X of Apo-deP, and k_{deP} the rate constant for the dephosphorylation. a = 0.9 in the experiments reported herein, minimizing the contribution of the second term. We denote the important comparison $k_{ex,P} - k_{ex,deP}$ as Δk_{ex}. Table S1 summarizes the proper choices of data fitting deduced from use of eq. S2 in different settings.

Eq. S2 indicates that when the Δk_{ex} difference in the HDX rates of the two phosphorylation states is small, then the first term of eq. S2 becomes small. When $\left|\frac{P}{Q}\right| < 0.2$, the term $Pe^{-(k_{ex,P}+k_{deP})t}$ becomes negilible compared to $Qe^{-k_{ex,deP}t}$. Therefore, the kinetic equation for this case of overlapped peaks simplifies to the single exponential decay $Qe^{-k_{ex,deP}t}$ needing no correction because $k_{ex,deP}$ was fitted and $k_{ex,deP} \approx k_{ex,P}$ (Table S1). This situation was recognized at residues where k_{obs} of Apo-P is similar to $k_{ex,deP}$ of Apo-deP.

In cases where phosphorylation causes $k_{ex,P}$ and $k_{ex,deP}$ to differ enough that $|\Delta k_{ex}|$ is enlarged compared to the dephosphorylation rate k_{deP}, the first term of eq. S2 becomes large compared to the second term. When $\left|\frac{Q}{P}\right| < 0.2$, $Qe^{-k_{ex,deP}t}$ becomes negligible compared to $Pe^{-(k_{ex,P}+k_{deP})t}$. In such cases, a single exponential decay with rate constants $k_{ex,P} + k_{deP}$ was observed. This was corrected by subtracting away k_{deP}.

It can be shown (either by derivation or grid search of $k_{ex,P}$ or $k_{ex,deP}$ values) that in the bi-exponential regime (where $0.2 < \left|\frac{P}{Q}\right| < 5$), inappropriate fitting of a single-exponential decay to the bi-exponential decay introduces tolerably little error to resulting estimates of ΔG_{HX}.

Chemical Denaturation

The chemical denaturation of Apo-P and Apo-deP was performed using urea as described (5) but with modifications. 1.3 μM enzyme stock solutions of proteins in 50 mM MOPS, pH 7.4, and 0.1 mM DTT were mixed with this same buffer containing 10 M urea to obtain final urea concentrations ranging up to 8 M. The mixtures were incubated for 12 h. (Longer incubation times give similar denaturation curves.) Trp fluorescence emission was excited at 280 nm and detected at 320 nm using a BioTek Synergy MX plate reader.

Molecular dynamics simulations

The crystal structures of the Apo-P and Apo-deP forms of PMM/PGM (PDB codes 1K35 and 4MRQ, respectively) provided the initial structures. All crystallographic waters were included in the simulations. Hydrogen and missing side chain atoms were added using xleap (6). The Amber ff99SB force field was applied to all residues except the metal binding site (7). The region around the metal-binding site was parameterized as described for the electrostatic calculations. The protonation of the enzyme was set by neutral pH with the pSer108 deprotonated, consistent with the catalytic mechanism (8). The simulations were carried out using GROMACS 4.5.5 (9, 10) on the high performance computing facility at the University of Missouri Bioinformatics Consortium. The enzyme coordinates were solvated in a 10 Å truncated octahedral box containing about 13,000 TIP3P waters and neutralized with Na^+ ions. Moderate Langevin dynamics with a collision frequency of r = 1 ps^{-1} were applied. The cutoff for non-bonded interactions was 10 Å. The SHAKE algorithm was applied (11). After initial minimization, stepwise heating to 10, 50, 100, 150, 200, 250, and 310 K (12) was performed. The system was equilibrated under constant volume for 100 ps and then under constant pressure for another 100 ps. The 60-ns production simulations used periodical boundary condition in an NPT ensemble. The temperature was maintained at 310 K and pressure 1 atm using Berendsen thermostat and Parrinello-Rahman barostat algorithms (13, 14), respectively.

HX protection simulated from MD trajectories

Previous efforts to simulate HX protection, i.e. $\ln(P_n^{sim})$, from simulations and structures assumed that the contributions of contacts and hydrogen bonding or RMSF^{-1} to the protection are identical for all residues (15-17). However, as each residue could have a unique environment, the contributions may vary. Therefore, we clustered all residues into two groups, those with more or less protection from measured hydrogen exchange. We optimized independent sets of β_C and β_H or $\beta_{1/RMSF}$ for these two clusters of residues, using the same type of optimization of the difference between $\ln(P_n^{sim})$ from unrestrained MD simulations and experimentally measured $\ln(P_n^{exp})$ as described by Kieseritzky et al (17), i.e. minimizing this RMS deviation:

$$\Delta lnP = \sqrt{\frac{1}{N}\sum_{n=1}^{N}\left(\ln(P_n^{sim}) - \ln(P_n^{exp})\right)^2} \quad \text{(eq. S3)}$$

Two alternative sets of βc and β_H for quickly or slowly exchanging sites turned out to better simulate the protections and minimize the overall ΔlnP than did a single set of coefficients, for a set of well-characterized model proteins and their structures (Table S3) and for the PMM/PGM enzyme and its MD trajectories (Table S4).

In the tallying of structural interactions for the optimization process, contacts N_n^c between two residues were defined when the distances between amide nitrogen and heavy atoms are closer than 6.5 Å (16). Hydrogen bonds N_n^h were considered as formed for H-O distances shorter than 2.4 Å and N-H-O angles greater than 140 °. The errors were calculated as the standard deviations of the time-averaged protection factor elements (PFEs, e.g. N_n^c and N_n^h) counted from the trajectories. Since well-protected amide groups should be observed by NMR-detected HDX, $\beta_c^{\text{less prot}}$ and $\beta_H^{\text{less prot}}$or $\beta_{1/RMSF}^{\text{less prot}}$ were used to calculate $\ln(P_n^{sim})$ of residues that were not detected by HDX or CLEANEX-PM in plotting Fig. 6C. The good correlations between $\ln(P_n^{sim})$ and $\ln(P_n^{exp})$ (Tables S3 and S4, Fig. S11 and 6B) suggest that $\ln(P_n^{sim})$ could be used as a proxy for $\ln(P_n^{exp})$ for the numerous amide groups of PMM/PGM in the unmeasured time regime of HX slower than 12 s and faster than 20 min; compare Fig. 3A and 6C.

Table S1. Behaviors of amide TROSY NMR peaks of Apo-P monitored by HDX and the appropriate data fitting method implemented.

Category	Count	Data Fitting
Total peaks of Apo-P tracked by HDX	155 (68%) *	
Residues with well-resolved peaks for Apo-P and Apo-deP	87 (38.2%)	Single exponential $k_{obs} = k_{ex,P} + k_{deP}$ †
Only Apo-P peaks present as Apo-deP peaks were missing	11 (4.8%)	Single exponential $k_{obs} = k_{ex,P} + k_{deP}$ †
Overlapped peaks	57 (36.7%)	
Apo-deP peak decayed too quickly to be seen by HDX-NMR. ‡	31 (13.6%)	Single exponential §‡ $k_{obs} = k_{ex,P} + k_{deP}$
Phosphorylation changes k_{ex} significantly: $\Delta k_{ex} < -3.6 k_{deP}$ or $\Delta k_{ex} > 12.5 k_{deP}$, $\left|\frac{\boldsymbol{Q}}{\boldsymbol{P}}\right| < \mathbf{0.2}$ ¶	13 (5.7%)	Single exponential $k_{obs} = k_{ex,P} + k_{deP}$ §
Little effect of phosphorylation: $\lvert\Delta k_{ex}\rvert < 0.22 k_{deP}$, $\left|\frac{\boldsymbol{P}}{\boldsymbol{Q}}\right| < \mathbf{0.2}$	13 (5.7%)	Single exponential $k_{obs} = k_{ex,P} = k_{ex,deP}$
$\mathbf{0.2} < \left|\frac{\boldsymbol{P}}{\boldsymbol{Q}}\right| < \mathbf{5}$	0 (0%)	Bi-exponential See eq. S2

[*] % of the total amide peaks monitored are given in parentheses

[†] Apparent k_{deP} values for each of these individual residues (individually fitted to the decay of each NMR peak in H_2O) were used to accommodate the anomalously fast decay of 14 of these 98 peaks (a group with time constant of 4.5 ± 0.1 h and "k_{deP}" of ~3.7×10^{-3} min^{-1}).

[‡] $k_{ex,deP}$ was rapid, apparently > 0.05 min^{-1}

[§] The globally fitted value of k_{deP} was used to correct the k_{ex} values of Apo-P.

[¶] $\Delta k_{ex} = k_{ex,P} - k_{ex,deP}$. P and Q are defined by eq. S2.

Table S2. NMR identification of residues with HX altered by Ser108 phosphorylation, clarifying behaviors within peptides obscured in HDX-MS results

	Peptide residues*	**Stabilized by phosphorylation**	**Destabilized by phosphorylation**	**Little change[†]**
Partly overlapping active site	92-117[‡]	92, 95,106,115,116	Not detected	93,97,98, 101,117
	205-239	223,239	206,219,230,236	221,225,228,229, 231-233
	240-266	244,247,263-266	242	245,252,253,255, 258,259,261
	267-293	268,269,271-273, 275,278,280-282,291	Not detected	270,279,289,292
	323-346	323,324,333,335,336	343, 345	331, 346
Far from active site				
	28-44	28,30,36,38,44	33,37,41	29,32,42,43
	45-52	Not detected	45,50	46,48
	53-78	59,63,64,66,72,77	58	55,65,75,78
	169-191	171,173,174,176, 178,180,183,185	184, 188	169,179,186,191
	192-204	195,197,198,	194,202,203	193,196,200
	378-406	378,381,384, 385,389, 392,404	Not detected	379,380,382,383,387, 391,393,397,398,399,403
	407-429	407,409,410,413, 416-422	Not detected	411,412,415,428,429
	442-463	442,446,448,449,455	Not detected	444,445,447, 451-454,457

* Peptides were generated by pepsinolysis. Percentage increase in deuteration of peptide as a whole was measured by mass spectrometry (18).

[†] Insufficient evidence of a difference greater than 1 kcal/mol

[‡] The phosphopeptide evaded detection by HDX-MS.

Table S3. Comparison of one and two sets of coefficients in modeling HX protection factors from surrounding contacts and hydrogen bonds for well-characterized proteins

Protein	**One pair of coefficients**				**Two pairs of coefficients**					
					less protected residues		**more protected residues**			
	β_C*	**β_H[†]**	**ΔlnP[‡]**	**Pearson's correlation coefficient**	β_C*	β_H[†]	β_C*	β_H[†]	**ΔlnP [‡]**	**Pearson's correlation coefficient**
Ubiquitin[§]	0.35[¶]	2.00[¶]	3.73	0.75	0.48	1.06	0.75	1.39	1.72	0.88
	0.58[‖]	2.30[‖]	2.33	0.75						
Staphylo-coccal nuclease[**]	0.35[¶]	2.00[¶]	2.07	0.64	0.13	0.79	0.35	1.26	1.19	0.85
	0.27[‖]	1.80[‖]	1.71	0.64						
bacterial cytochrome c [††]	0.35[¶]	2.00[¶]	3.04	0.58	0.51	0.36	0.65	0.28	1.57	0.77
	0.60[§§]	1.59[§§]	1.86[§§]	0.62[§§]						

* Coefficient for the number of contacts surrounding each residue (15)

[†] Coefficient for the number of hydrogen bonds to each backbone amide group (15)

[‡] Difference in natural logarithm of simulated and experimental protection factor P (15); smaller indicates better agreement.

[¶] Optimized in ref (16)

[‖] Parameters optimized for measured HX protection factors following the method of ref (17).

[§§] From ref (17)

[§] Protection factors were calculated from rates of HX of ref (19). PDB: 1UBI

** HX protection factors from ref (3). PDB: 1SNO. Hydrogen atoms were added to the coordinates using Sybyl 7.3.

[††] HX protection factors are digitized from Fig. 2 of ref (20), PDB: 1K3G (first conformer).

Table S4. Comparison of HX protection factors measured and simulated from MD trajectories, ΔlnP, of PMM/PGM, using one or two pairs of coefficients for protection factor elements (PFE)

Phosphorylation state	**PFE1, no. of contacts**	**PFE2**	**less protected residues**		**more protected residues**		ΔlnP	**Pearson's correlation coefficient**
			β_c	β_2	β_c	β_2		
Apo-P	N_n^c	N_n^h	0.35	2.0*	0.35	2.0*	6.7	0.34
Apo-deP							5.5	0.36
Apo-P	N_n^c	N_n^h	0.22	0.68	0.80	2.50	3.2	0.82
Apo-deP							2.6	0.89
Apo-P	N_n^c	RMSF^{-1}	0.22	0.28†	0.56	3.94†	3.1	0.83
Apo-deP							2.7	0.88

* The single pair of coefficients optimized by ref (16) was applied and is listed twice.

† These two pairs of coefficients were used to generate Fig. 6, B and C.

Supporting References

1. Hwang, T. L., P. C. van Zijl, and S. Mori. 1998. Accurate quantitation of water-amide proton exchange rates using the phase-modulated CLEAN chemical EXchange (CLEANEX-PM) approach with a Fast-HSQC (FHSQC) detection scheme. Journal of Biomolecular NMR 11:221-226.
2. Huyghues-Despointes, B. M., J. M. Scholtz, and C. N. Pace. 1999. Protein conformational stabilities can be determined from hydrogen exchange rates. Nat. Struct. Biol. 6:910-912.
3. Skinner, J. J., W. K. Lim, S. Bedard, B. E. Black, and S. W. Englander. 2012. Protein hydrogen exchange: testing current models. Protein Sci. 21:987-995.
4. Zhu, G., Y. Xia, L. K. Nicholson, and K. H. Sze. 2000. Protein Dynamics Measurements by TROSY-Based NMR Experiments. J. Magn. Reson. 143:423-426.
5. Fulcher, Y. G., and S. R. Van Doren. 2011. Remote exosites of the catalytic domain of matrix metalloproteinase-12 enhance elastin degradation. Biochemistry 50:9488-9499.
6. Case, D. A., T. A. Darden, T. E. Cheatham, C. L. Simmerling, J. Wang, R. E. Duke, R. Luo, R. C. Walker, W. Zhang, K. M. Merz, B. Roberts, S. Hayik, A. Roitberg, G. Seabra, J. Swails, A. W. Goetz, I. Kolossváry, K. F. Wong, F. Paesani, J. Vanicek, R. M. Wolf, J. Liu, X. Wu, S. R. Brozell, T. Steinbrecher, H. Gohlke, Q. Cai, X. Ye, M. J. Hsieh, G. Cui, D. R. Roe, D. H. Mathews, M. G. Seetin, R. Salomon-Ferrer, C. Sagui, V. Babin, T. Luchko, S. Gusarov, A. Kovalenko, and P. A. Kollman. 2012. AMBER 12. University of California, San Francisco.
7. Hornak, V., R. Abel, A. Okur, B. Strockbine, A. Roitberg, and C. Simmerling. 2006. Comparison of multiple Amber force fields and development of improved protein backbone parameters. Proteins: Structure, Function, and Bioinformatics 65:712-725.

8. Naught, L. E., and P. A. Tipton. 2001. Kinetic Mechanism and pH Dependence of the Kinetic Parameters of *Pseudomonas aeruginosa* Phosphomannomutase/Phosphoglucomutase. Archives of Biochemistry and Biophysics 396:111-118.
9. Berendsen, H. J. C., D. van der Spoel, and R. van Drunen. 1995. GROMACS: A message-passing parallel molecular dynamics implementation. Comput. Phys. Commun. 91:43-56.
10. Lindahl, E., B. Hess, and D. van der Spoel. 2001. GROMACS 3.0: a package for molecular simulation and trajectory analysis. J Mol Model 7:306-317.
11. Ryckaert, J.-P., G. Ciccotti, and H. J. C. Berendsen. 1977. Numerical integration of the cartesian equations of motion of a system with constraints: molecular dynamics of n-alkanes. Journal of Computational Physics 23:327-341.
12. Xu, J., G. Yin, and W. Du. 2011. Distal mutation modulates the heme sliding in mouse neuroglobin investigated by molecular dynamics simulation. Proteins 79:191-202.
13. Berendsen, H. J. C., J. P. M. Postma, W. F. van Gunsteren, A. DiNola, and J. R. Haak. 1984. Molecular dynamics with coupling to an external bath. J. Chem. Phys. 81:3684-3690.
14. Parrinello, M., and A. Rahman. 1981. Polymorphic transitions in single crystals: A new molecular dynamics method. J. Appl. Phys. 52:7182-7190.
15. Vendruscolo, M., E. Paci, C. M. Dobson, and M. Karplus. 2003. Rare fluctuations of native proteins sampled by equilibrium hydrogen exchange. J. Am. Chem. Soc. 125:15686-15687.
16. Best, R. B., and M. Vendruscolo. 2006. Structural Interpretation of Hydrogen Exchange Protection Factors in Proteins: Characterization of the Native State Fluctuations of CI2. Structure 14:97-106.
17. Kieseritzky, G., G. Morra, and E.-W. Knapp. 2006. Stability and fluctuations of amide hydrogen bonds in a bacterial cytochrome c: a molecular dynamics study. J. Biol. Inorg. Chem. 11:26-40.
18. Lee, Y., M. T. Villar, A. Artigues, and L. J. Beamer. 2014. Promotion of Enzyme Flexibility by Dephosphorylation and Coupling to the Catalytic Mechanism of a Phosphohexomutase. J. Biol. Chem. 289:4674-4682.
19. Bougault, C., L. Feng, J. Glushka, E. Kupče, and J. H. Prestegard. 2004. Quantitation of rapid proton-deuteron amide exchange using hadamard spectroscopy. J. Biomol. NMR 28:385-390.
20. Bartalesi, I., A. Rosato, and W. Zhang. 2003. Hydrogen exchange in a bacterial cytochrome c: a fingerprint of the cytochrome c fold. Biochemistry 42:10923-10930.